Operando Probing Dynamic Migration of Copper Carbonyl During Electrocatalytic CO_2 Reduction

Yao Yang,[1,2,3,4,†] Julian Feijóo,[1,3,†] Marc Figueras-Valls,[5,†] Chubai Chen,[1,3,†] Chuqiao Shi,[6] Maria V. Fonseca Guzman,[1,3] Yves Murhabazi Maombi,[7] Shikai Liu,[4] Pulkit Jain,[7] Valentín Briega-Martos,[4] Zhengxing Peng,[8] Yu Shan,[3,9] Geonhui Lee,[1] Michael Rebarchik,[5] Lang Xu,[5] Christopher J. Pollock,[10] Jianbo Jin,[1] Nathan E. Soland,[1] Cheng Wang,[8] Miquel B. Salmeron,[9,11] Zhu Chen,[7] Yimo Han,[6] Manos Mavrikakis,[5,*] Peidong Yang[1,3,9,11,12*]

[1]Department of Chemistry, University of California, Berkeley, CA 94720, USA
[2]Miller Institute for Basic Research in Science, University of California, Berkeley, CA 94720, USA.
[3]Chemical Sciences Division, Lawrence Berkeley National Laboratory, Berkeley, CA 94720, USA.
[4]Department of Chemistry and Chemical Biology, Cornell University, Ithaca, NY 14850, USA.
[5]Department of Chemical and Biological Engineering, University of Wisconsin-Madison, Madison, WI 53706, USA.
[6]Department of Materials Science and NanoEngineering, Rice University, Houston, TX 77005, USA
[7]Department of Chemical Engineering, University of Massachusetts Amherst, Amherst, MA 01003, USA
[8]Advanced Light Source, Lawrence Berkeley National Laboratory, Berkeley, CA 94720, USA.
[9]Department of Materials Science and Engineering, University of California, Berkeley, CA 94720, USA.
[10]Cornell High Energy Synchrotron Source, Cornell University, Ithaca, NY 14850, USA.
[11]Materials Sciences Division, Lawrence Berkeley National Laboratory, Berkeley, CA 94720, USA.
[12]Kavli Energy NanoScience Institute, Berkeley, CA 94720, USA.
*Corresponding authors: p_yang@berkeley.edu; emavrikakis@wisc.edu
†Y.Y., J.F., M.F.V. and C.C. contributed equally.

Abstract:

Single crystals and shape-controlled nanocrystals are well-known to exhibit facet-dependent catalytic properties. However, few reports have investigated how those nanocrystals evolve and (de)activate under reaction conditions, calling for developing nanoscale time-resolved *operando* methods. Here, we design Cu nanocubes as a model system to elucidate the underlying driving force of dynamic nanocatalyst reconstruction during CO_2 reduction reaction (CO_2RR). *Operando* electrochemical liquid-cell scanning transmission electron microscopy (EC-STEM) and synchrotron-based X-ray spectroscopy reveal the size- and potential-dependent complete transformation from (100)-oriented Cu@Cu_2O nanocubes to polycrystalline metallic Cu nanograins under CO_2RR. Machine-learning-assisted *operando* four-dimensional STEM reveals that large cube-derived Cu nanograins form mainly crystalline domains while small counterparts are more amorphous due to faster evolution kinetics. *In situ* Raman spectroscopy and density functional theory calculations suggest that CO ejects single Cu atoms, resulting in few-nm Cu clusters and surface migration of highly mobile copper carbonyl (Cu-CO) species. These joint multimodal *operando* method-theory approaches pave the way for understanding complex structural evolution of energy-related nanocatalysts under electrochemical conditions.

Introduction:

Advances in the design of catalysts require an atomic/molecular-level understanding of the dynamic nature of active sites under operating conditions[1-3]. Among a variety of renewable energy and environmental applications, CO_2 electroreduction on copper catalysts is a cornerstone reaction to achieve carbon neutrality with the potential to fix CO_2 into valuable multi-carbon (C_{2+}) fuels and chemicals[4-7]. Our recent *operando* studies investigated the dynamic evolution of Cu nanocatalysts into metallic Cu nanograins as active sites for selective CO_2 reduction reaction (CO_2RR).[8-11] Recent molecular dynamic simulations revealed that oxide-derived Cu would be fully reduced to metallic Cu under electrochemical CO_2 reduction.[12] Other studies also suggested that Cu catalysts experienced significant reconstruction and morphological/structural changes under reaction conditions[13-15]. Since the pioneering studies by Hori et al. showed facet-dependent CO_2RR selectivity on bulk Cu single-crystal electrodes[16-17], dynamic reconstruction of single-crystal surfaces has been extensively investigated. Gas-phase scanning tunneling microscopy (STM), X-ray photoelectron spectroscopy (XPS), and density functional theory (DFT) calculations revealed that Cu atom migration and nanocluster formation were driven by CO binding to low-coordinated Cu atoms[18-22]. Those studies proposed the formation of a Cu-CO complex, which weakened the binding of Cu to its neighboring Cu atoms, thereby enabling the ejection of Cu atoms leading to Cu cluster formation [19,20]. Recent *in situ* electrochemical liquid-phase STM and atomic force microscopy (AFM) studies investigated CO-induced Cu cluster formation and migration on bulk polycrystalline and single-crystal Cu electrodes under relevant CO_2RR conditions[23-26]. Those studies indicate that CO, one of the major CO_2RR products, plays a significant role in modulating the dynamic nature of Cu active sites. Cu-CO species were first reported in the 1920s[27-31] and extensively studied as copper carbonyl complexes ($Cu(CO)_x$ (x=1-3)) in the gas phase by vibrational spectroscopy since the 1970s[32-34]. Such species have been recently suggested to exist in solution under open circuit potentials[35]. However, the formation/migration and nature/identities of Cu-CO species at/near catalytic surfaces under electrochemical conditions remain largely elusive. Detailed studies of such phenomena are of significant interest for mechanistic understanding of the dynamic evolution of Cu nanocatalysts.

To bridge the knowledge gap between bulk single-crystal electrodes and practical nanoparticle catalysts, shape-controlled nanocrystals have emerged as an important family of nanomaterials since they exclusively expose certain facets to achieve tunable catalytic activity/selectivity[36,37]. At this length scale (1-100 nm), the properties of nanocatalysts may deviate significantly from their bulk single-crystal counterparts, leading to additional tunability for establishing structure-(re)activity relationships. Shape-controlled nanocrystals are expected to experience a significantly higher level of reconstruction when compared to bulk single-crystal electrodes[38-40]. While there are numerous studies on the synthesis of shape-controlled nanocrystals and characterization of their pristine structures[36,37], only a few studies have investigated how they (de)activate and evolve under electrochemical conditions[12-14]. However, those studies suggest that shape-controlled nanocrystals, characterized *ex situ*, may not maintain the same structures and properties but evolve into significantly different structures under operating conditions[38-40]. Given the dimensions of nanocrystals, their study necessitates the development of nanoscale, time-resolved *operando* methods for catalyst characterizations under electrochemical conditions[41-43].

In this work, we design (100)-oriented Cu nanocubes as a model catalyst system since early studies on bulk Cu(100) single crystals showed significantly higher CO_2RR selectivity for C_2H_4 than Cu(111)[16,17]. Previous *ex situ*[12] and *in situ*[13,14] studies observed incomplete reconstruction of Cu nanocubes with mild surface roughening, nanoclustering or fragmentation, and concomitant

decay in multi-carbon selectivity over time. Here, we employ *operando* EC-STEM to investigate the dynamic structural transformation of 55 and 27 nm Cu cubes during the CO_2RR. Both sized cubes undergo complete reconstruction to metallic Cu nanograins while maintaining a high C_2H_4 selectivity and achieve steady-state performance over extended periods of time. *Operando* electrochemical four-dimensional (4D)-STEM, assisted by machine learning (ML), was used to interrogate the complex nature of polycrystalline active sites. DFT calculations and *operando* Raman spectroscopy show that CO intermediates can electrochemically drive Cu migration during CO_2RR. The multimodal structural and molecular investigation presented in this work suggests that CO is the key intermediate to induce the formation of mobile Cu-CO species at/near catalyst surfaces and drives dynamic Cu cluster formation and migration under CO_2RR.

Results:

Overview of size- and potential-dependent structural evolution pathways

Monodisperse Cu nanocubes were prepared by colloidal synthesis (Supplementary Table 1) to investigate their potential- and size-dependent structural evolution during the CO_2RR. The schematic overview in Figs. 1a-b summarizes the key steps of the evolution pathway. As-synthesized larger (55 nm) and smaller (27 nm) nanocubes have a metallic Cu core (yellow) and a Cu_2O shell (green). The surface oxide of the 55 nm nanocubes experiences an electroreduction at 0 V and forms a metallic, amorphous and low-density spongy shell (coating) in yellow (Fig. 1a). During subsequent CO_2RR at -1.0 V, the spongy shell first nucleates and grows into Cu seeds (step 1) followed by a subsequent evolution of the cubic core (step 2) and achieves a steady state of metallic polycrystalline Cu nanograins (step 3). In comparison, smaller (27 nm) cubes also form a spongy shell but with an incomplete coating around the cubic Cu core (Fig. 1b). The cubic core of 27 nm Cu evolves first followed by the migration of the spongy shell (steps 1-2) and reaches a steady state of polycrystalline Cu nanograins. The section in the dashed circle in Fig. 1a corresponds to the molecular picture of ejection of single-atom Cu and migration of Cu-CO forming few-nm Cu clusters during dynamic evolution of Cu nanocatalysts. The difference in the stepwise evolution pathway of both Cu nanocubes can be rationalized by a higher reactivity of the smaller cubic Cu core (27 nm), which results in faster and more disordered evolution kinetics and has a significant impact on the structures and CO_2RR selectivity of resulting Cu nanograins.

High-angle annular dark-field STEM (HAADF-STEM) images show that the as-synthesized nanocubes have a well-defined cubic morphology with sizes of 55 ± 6.0 and 27 ± 1.6 nm (Figs. 1c,g, Supplementary Figures 1-2). Corresponding electron energy loss spectroscopy (EELS) maps reveal that Cu nanocubes of both sizes exhibit a metallic Cu core (yellow) surrounded by a ~2 nm (*i.e.*, ~8-atomic-layer) Cu_2O shell (green, Figs. 1d,h, Supplementary Figures 3-4). Atomic-scale STEM images resolve that the metallic Cu core has a single-crystal structure with d-spacings of Cu{200} (1.8 Å) on the [001] zone axis of Cu while the Cu_2O shell is polycrystalline with d-spacings of Cu_2O{111} (2.5 Å) (Figs. 1e,i, Supplementary Figures 5-6). The ~2 nm Cu_2O shell is formed right after synthesis and self-passivated during extended storage in air (Supplementary Figures 3, 7). The *ex situ* STEM-EELS analysis shows that the Cu nanocubes have a single-crystal Cu core surrounded by a polycrystalline Cu_2O shell ($Cu@Cu_2O$), which provides a baseline understanding for in-depth *operando* EC-STEM studies.

***Operando* EC-STEM studies of morphological changes**

Operando EC-STEM imaging was used to track the dynamic morphological evolution of Cu

nanocubes under CO_2RR. An EC-STEM liquid cell has a three-electrode system including as-synthesized Cu nanocubes deposited on a carbon working electrode (WE) with a Pt counter and pseudo-reference electrode (CE and RE)[43,44]. A linear sweep voltammetry (LSV) from 0.4 to around 0.0 V vs. the reversible hydrogen electrode (RHE) is applied to trigger electrogenerated hydrogen bubbles (all potentials are converted to the RHE scale[8] unless otherwise noted). Hydrogen bubbles are naturally formed during CO_2RR and enable a thin-liquid film (~100 nm) that improves the spatial resolution in EC-STEM imaging while remaining electrochemically accessible to nanocatalysts on the carbon WE. The 55 nm nanocubes develop a spongy shell surrounding the perimeter of the cubic structures (Fig. 1f), likely from the electroreduction of the Cu_2O shell of pristine nanocubes. In comparison, 27 nm nanocubes develop a similar but incomplete spongy shell, possibly due to the higher reactivity of the Cu_2O shell of smaller cubes (Fig. 1j), which resembles the melting Cu feature of 18 nm spherical Cu nanoparticle ensembles in our recent study[8] under similar CO_2RR conditions (Supplementary Figure 8). To rigorously ascribe the formation of the Cu spongy shell to the electroreduction of the Cu_2O shell, a series of control experiments were performed. Only 55 nm cubes on the carbon WE formed a spongy shell while other cubes away from the WE under beam exposure did not form a spongy shell, which suggests that the formation of a spongy shell is driven by electrochemical reduction rather than possible beam-induced growth (Supplementary Figure 9). Inductively coupled plasma optical emission spectroscopy (ICP-OES) measurements were performed to rule out the possibility of electrodeposition of residual Cu species in hexane supernatant during colloidal synthesis and sample preparation (Supplementary Figure 10). Particle size distribution (PSD) analyses of both pristine and electroreduced 55 and 27 nm nanocubes after LSV scans suggest that the decrease in the average sizes of the cubic cores is consistent with the removal of the 2 nm Cu_2O shell (Supplementary Figures 11-12). The trioctylphosphine oxide (TOPO) ligand has a weak interaction with as-synthesized Cu nanocube surfaces and is expected to experience a similar ligand desorption to that of the tetradecylphosphonic acid (TDPA) ligand of 7 nm Cu NPs in previous reports,[45,46] which rules out the possibility of spongy shell being organic ligands. Finally, *operando* X-ray absorption spectroscopy shows that 27 nm cubes become fully metallic Cu at 0 V, which supports that the spongy shell, formed at 0 V, is metallic Cu (Supplementary Figure 13). In light of all the above experimental results, we conclude that the spongy shell is metallic Cu from electroreduction of the Cu_2O shell of pristine $Cu@Cu_2O$ nanocubes.

A routine beam-dose control experiment was performed for each EC-STEM video to ensure that structural evolution is driven by electrochemical potential without beam damage (Fig. 2, Supplementary Figures 14-17, Supplementary Videos 1-5). At a mild reducing potential (*i.e.*, chronoamperometry, CA) of 0 V for 120 s, the spongy shell of 55 nm nanocubes experienced progressive evolution while the cubic Cu core remained largely unchanged (Figs. 2a-d). Concomitantly, small spherical Cu nanograins (10-20 nm) nucleated and further evolved into Cu nanograins (~50 nm) at locations adjacent to those remaining cubes (Fig. 2d, Supplementary Figure 14, Supplementary Video 1). At a typical CO_2RR potential of -1 V, the cubic Cu cores experienced further evolution into Cu nanograins with an increase in both quantity and particle sizes (Fig. 2e-h, Supplementary Figure 15, Supplementary Video 2). In contrast to the evolution of 55 nm nanocubes (spongy shell followed by cubic core), 27 nm nanocubes experienced the opposite evolution of the cubic core followed by the spongy shell (Fig. 2i-p, Supplementary Video 3). The initial spongy shell around the remaining 27 nm cubic Cu core is incomplete with a more random distribution than that of the 55 nm cubic Cu core (Fig. 2i). From 4 to 20 s at -1 V, the cubic Cu core experienced progressive evolution (marked by dashed circles in Figs. 2j,n) with

simultaneous growth of irregular Cu nanograins (marked by dashed rectangles). From 20 to 80 s, the spongy shell underwent further evolution, leading to larger and more abundant Cu nanograins (Figs. 2n-p). The opposite stepwise evolution behaviors of 55 nm cubes (spongy shell followed by cubic core) and 27 nm cubes (cubic core followed by the spongy shell) were further confirmed in other regions (Supplementary Figures 16-17, Supplementary Videos 4-5) and were ascribed to the faster evolution kinetics of smaller cubes (27 nm).

ML-assisted *operando* 4D-STEM analysis of nanograins

Moving beyond conventional STEM images of morphological changes, *operando* electrochemical 4D-STEM diffraction imaging enables structural analysis of the complex nature of polycrystalline Cu nanograins under CO_2RR (Fig. 3). 4D-STEM is based on the principle of recording a two-dimensional (2D) electron diffraction pattern over a 2D grid of probe positions. The recent development of an electron microscope pixel array detector (EMPAD) enables 4D-STEM diffraction imaging to retrieve nm-scale structural information at a much lower beam dose, which is indispensable for beam-sensitive nanocatalysts in liquid[47,48]. Unsupervised machine learning, based on k-means hierarchical clustering[49,50], was used to segment the complex 4D-STEM dataset into subgroups with different crystal orientations (Supplementary Figure 18). Although both 55 and 27 nm cube-derived Cu nanograins display similar polycrystalline features (Figs. 3a,d), those Cu nanograins exhibit significantly different distributions of crystalline and amorphous/disordered domains (Figs. 3b,e). The results are shown as false-color 4D-STEM maps, where different colors represent different crystallinity of Cu domains. The number increases from 0 in black (representing SiN_x/liquid background) to 1 in grey (representing nearly amorphous/disordered Cu domains) and 2-11 in other colors (crystalline Cu domains). 55 nm cube-derived nanograins are mainly composed of polycrystalline Cu domains (Figs. 3b-c). In contrast, the majority of 27 nm cube-derived nanograins are nearly amorphous/disordered in grey (numbers 1-2), in addition to other crystalline nanograins in colors with numbers 3-11 (Figs. 3e-f). To quantify the relative degree of crystallinity of polycrystalline Cu domains, fluctuation electron microscopy (FEM) analysis[51] was performed to study medium-range ordering in disordered materials (Supplementary Figure 19a,b). The FEM analysis can distinguish crystalline Cu domains with a higher contrast when compared to amorphous Cu ones (Supplementary Figures 19c,d), confirming the presence of domains with varying degrees of crystallinity. 4D-STEM analysis shows that the spongy Cu shell is primarily an amorphous coating surrounding the remaining crystalline Cu nanocubes (Supplementary Figure 20). With a probe size of around 1 nm, nanograin boundaries with different crystallographic orientations were resolved among 55 nm cube-derived crystalline domains (Supplementary Figures 21-22) and 27 nm cube-derived crystalline and amorphous domains (Supplementary Figures. 23-24). In summary, 27 nm cube-derived Cu nanograins have a larger contribution of amorphous/disordered domains when compared to 55 nm cube-derived nanograins with more crystalline domains. This is in agreement with the faster and more disordered structural evolution of smaller and thus more reactive 27 nm cubes, relative to larger (55 nm) cube counterparts, as revealed in previous EC-STEM images (Figs. 1a,b and 2).

***Operando* hard X-ray spectroscopy of valence state changes**

Operando high-energy-resolution fluorescence-detected (HERFD) X-ray absorption spectroscopy (XAS) was employed to track the time-resolved changes of the valence state of Cu active sites during the CO_2RR. HERFD XAS selectively detects Cu $K_{\alpha 1}$ emission lines and achieves a significantly higher energy resolution (~0.5 eV) than conventional XAS (~1.5 e V), which enables the detection of fine pre-edge features in the X-ray absorption near-edge structure

(XANES).[8,9] *Operando* HERFD XANES of 55 nm and 27 nm cubes show the reduction of surface Cu_2O to metallic Cu under CO_2RR (red arrow) and partial reoxidation of metallic Cu to Cu_2O upon air exposure (green arrow) (Fig. 4a, Supplementary Figures 25-26). A linear combination fitting (LCF) quantitative analysis shows that 55 and 27 nm Cu@Cu_2O cubes have 14% and 26% Cu_2O, respectively, with a relative fitting error of <1% (Supplementary Figures 27-28). This finding matches well the relative fraction of Cu_2O expected from ~2 nm oxide shell identified through the EELS analysis (Supplementary Figure 29). *Operando* HERFD XANES was used to quantify the relative fraction of metallic Cu as a function of the time under CO_2RR and subsequent air exposure (Fig. 4b). Pristine 55 nm Cu@Cu_2O nanocubes experienced a complete conversion of 14% Cu_2O to fully metallic Cu nanograins within 10 min of CO_2RR at -1.0 V vs. RHE (Fig. 4b, red line). When the applied potential was released after 1 h of electroreduction, metallic Cu nanograins experienced partial reoxidation and formed about 12% Cu_2O (Fig. 4b, green line). In comparison, 27 nm Cu@Cu_2O nanocubes experienced a similar conversion of 26% Cu_2O to fully metallic Cu during CO_2RR followed by the formation of a larger fraction of around 35% Cu_2O after the bias was released (Figs. 4c-d). This is consistent with a thicker oxide shell (~4 nm) of 27 nm cube-derived Cu nanograins than that of 55 nm cube-derived Cu nanograins (~2 nm) after air exposure (Supplementary Figures 30-31). To track the time-resolved electroreduction and reoxidation of Cu cubes, the incident X-ray photon energy was fixed at 8979.5 eV where the relative signal intensity corresponding to valence changes achieves a maximum value. 55 nm nanocubes required 120 s for a complete reduction of surface Cu_2O, about 30 s longer than smaller 27 nm nanocubes (90 s) as shown in Supplementary Figure 32. The electroreduction/reoxidation cycles of 55 and 27 nm cubes were also confirmed by *operando* extended X-ray absorption fine structure (EXAFS) analysis (Supplementary Figures 33-34).

Operando soft X-ray scattering of interparticle dynamics

Operando electrochemical resonant soft X-ray scattering (EC-RSoXS),[52] using the same liquid-cell set-up as *operando* EC-STEM, was used to provide a complementary analysis on interparticle dynamics of large ensembles of Cu nanoparticles (Figs. 4e-f). Quantitative RSoXS analysis of pristine 55 nm Cu cubes suggests an average particle-particle distance of 5.8 ± 1.6 nm (Supplementary Figure 35), which is consistent with the distance estimated from STEM images (Supplementary Figure 1). As apparent from the positive shift of the first maximum (marked by dashed lines at ~0.1 nm^{-1}), the average particle-particle distance of metallic Cu nanograins decreases to 2.7 ± 1.8 nm at -1 V (Supplementary Figures 35), suggesting significant aggregation and reconstruction of Cu domains during the CO_2RR. In addition, the increase of scattering intensity at a low q-value (~0.07 nm^{-1}), marked by the blue arrow (Fig. 4e), indicates a higher degree of particle aggregation per unit area as an effect of denser packing. In summary, *operando* RSoXS provides complementary information to hard XAS on interparticle dynamics with an increasing level of particle aggregation under the CO_2RR.

Ex situ validation with benchtop experiments

It is commonly questioned whether the structural evolution observed in a special liquid-cell EC-STEM can faithfully represent what occurs in a standard three-electrode electrochemical cell. Extensive post-electrolysis scanning electron microscopy (SEM) imaging was performed to track the dynamic evolution of Cu nanocubes during the CO_2RR at -1 V for extended periods of time in an H-cell (Figs. 5a-d). As-synthesized 55 nm nanocubes exhibited the initial formation of Cu nanograins near remaining nanocubes after 30 min CO_2RR (Fig. 5b, Supplementary Figures 36).

The etching of 55 nm Cu cubes in an H-cell was clearly captured by SEM imaging after 30 min CO_2RR (Fig. 5b inset, Supplementary Figure 37), which resembled the etching features of Cu cubes in *operando* EC-STEM images (Figs. 5e-f, Supplementary Figure 38). 55 nm Cu nanocubes experienced a complete evolution into Cu nanograins after 2 h and further aggregation after 15 h (Figs. 5c-d, Supplementary Figure 39). A similar evolution from 27 nm nanocubes to polycrystalline Cu nanograins was observed, although the complete evolution of the smaller nanocubes only required 30 min when compared to 2 h for 55 nm nanocubes (Supplementary Figures 40-41). This is consistent with the faster evolution of smaller cubes observed in EC-STEM images (Fig. 2). Overall, *operando* EC-STEM and *ex situ* SEM images of nanocubes evolved in an H-cell are highly consistent in both etching features of cubes and complete evolution from cubes to irregular polycrystalline Cu nanograins (Figs. 5b,e). This comparison indicates that the structural evolution observed in *operando* EC-STEM images can faithfully represent what occurred in an H-cell. Structural evolution in the H-cell occurred at a timescale of 0.5-2 h while it only required 1-2 min in EC-STEM, which was ascribed to the much stronger local electrical field[43] in a confined thin-liquid configuration of EC-STEM setup (Supplementary Figure 42). The progressive structural evolution of 55 nm nanocubes for 2 h may also explain why the C_2H_4 Faradaic efficiency of 55 nm nanocubes reaches a plateau after 2 h of CO_2RR (Fig. 5g). 55 nm Cu nanocubes achieve a steady-state CO_2RR selectivity of about 40% C_{2+} products at -1 V vs. RHE in CO_2-saturated 0.1 M $KHCO_3$ in an H-cell and remain stable for extended periods of time (Supplementary Figures 43-44, Supplementary Table 2). As a proof of concept in industrially relevant operating conditions, practical membrane electrode assembly (MEA) measurements of 55 nm Cu nanocubes exhibited a higher C_{2+} selectivity (78%) and C_2H_4 selectivity (47%) at a large current density (300 mA/cm^2, Supplementary Figure 45, Supplementary Table 3). *Ex situ* SEM images of Cu nanocubes after MEA operation exhibit a similar structural reconstructions to those observed in EC-STEM and H-cell measurements (Supplementary Figure 45).

Different species adsorbed at the nanocube surface likely play an important role in the evolution kinetics. During the CO_2RR, the most important species to consider based on their binding energies to the Cu surface are *H, *CO, and *C_2H_4[13,20]. To investigate the influence of these species, a series of control experiments were performed: Firstly, nanocubes evolved in Ar-saturated phosphate buffer (0.1 M K_2HPO_4/KH_2PO_4), where only H* can adsorb on the cubes. Then, nanocubes evolved in CO-saturated 0.1 M $KHCO_3$, where both H* and *CO can co-adsorb. Finally, nanocubes evolved in C_2H_4-saturated phosphate buffer, where both H* and *C_2H_4 can co-adsorb. Based on extensive *ex situ* SEM imaging analysis (Supplementary Figures 46-49, Supplementary Table 4), the absence of CO significantly slows down Cu migration while the addition of CO notably accelerates Cu migration. The presence of C_2H_4 shows a similar effect to the Ar-saturated counterpart, indicating that C_2H_4 does not play a significant role in the Cu migration process. Therefore, those studies indicate that CO is the species driving the Cu migration and structural evolution. In addition, the presence of CO itself without external bias did not trigger Cu migration (Supplementary Figure 50), suggesting that electrical fields under negative potentials are necessary to trigger electrochemical CO-driven Cu migration. *Ex situ* SEM images show that the migration of Cu cubes on Cu bulk foil shows similar behavior to that of Cu cubes on carbon paper (Supplementary Figure 51), which motivates our subsequent DFT calculations for Cu atom migration on a pure Cu substrate. In summary, extensive *ex situ* SEM imaging analysis demonstrates a similar and complete structural evolution from Cu nanocubes to polycrystalline metallic Cu nanograins in an H-cell when compared to *operando* EC-STEM analysis. Systematic control experiments with the presence and absence of CO and applied potentials, respectively,

indicate that CO as a critical intermediate to drive Cu migration and the possible presence of copper carbonyl (Cu-CO) species.

Operando methods providing molecular evidence of Cu-CO

In order to provide direct molecular evidence of the migration of copper carbonyl species, *in situ* surface-enhanced Raman spectroscopy (SERS) was performed. In the present study of Cu nanocatalysts, the broad Raman peaks at around 2000-2100 cm^{-1} mainly come from CO adsorption on different Cu active sites (various facets, steps and terraces) and dynamically evolving Cu nanocatalyst surfaces (Supplementary Figure 52). Supplementary Table 5 provides a comprehensive literature summary of *operando*/*in situ* vibrational Raman/IR spectroscopy of CO stretch band frequency of a large library of nanoscale and bulk Cu electrocatalysts under a wide range of applied potentials and experimental conditions. This summary shows that the Raman/IR peaks of nanoscale or bulk Cu catalysts are all located in the broad range of 2000-2100 cm^{-1}. The broad CO stretch band is an inherent property of highly dynamic Cu surfaces with constantly reconstructing Cu facets, steps, and terraces, which were referred to as stochastic CO vibrations.[53] The literature survey indicates that it is unlikely to reliably distinguish individual copper carbonyl (Cu-CO) species, such as *CO on single-atom Cu or isolated few-nm Cu clusters, from larger (10-100 nm) Cu nanograins, bulk single-crystal or polycrystalline Cu films. Thus, we need to design a model catalyst to allow the controlled formation of different sized Cu clusters from single Cu atoms under the CO_2RR.

Here, we synthesized copper phthalocyanine (CuPc) catalysts supported on carbon nanotube (CNT) substrate, adapted from a previous report,[54] as a model system to investigate the CO-driven ejection of single-atom Cu and subsequent formation and migration of Cu clusters under CO_2RR-relevant conditions (Fig. 6a). Atomic-scale HAADF-STEM images show individual Cu atoms (highlighted in dashed circles) in pristine CuPc catalysts (Figs. 6b, Supplementary Figure 53). After CO_2RR electrolysis at -1 V vs. RHE for 1 h, *ex situ* STEM images reveal the formation of sub-1 nm Cu clusters with 3-4-atom Cu clusters and the co-existence of the remaining single Cu atoms (Supplementary Figure 54). The majority of Cu clusters have sizes of 1-3 nm with the characteristic d-spacings of Cu(111) (2.1 Å) and Cu{200} (1.8 Å) (Figs. 6c, Supplementary Figure 55) with some Cu clusters growing into 3-5 nm or bigger Cu nanograins (nanoparticles) (Figs. 6d, Supplementary Figure 55). Overall, atomic-scale STEM images indicate that single Cu atoms in CuPc catalysts were ejected by CO intermediates and evolved into few-nm Cu clusters during the CO_2RR.

Operando HERFD-XAS was performed to obtain ensemble-level information about the chemical and structural evolution of CuPc catalysts during the CO_2RR (Figs. 6e-h). As-synthesized CuPc catalysts are mainly Cu^{2+} based on the sharp feature at 8985 eV when compared to reference spectra (Supplementary Figure 56a). *Operando* HERFD XANES reveals a pronounced intensity increase of the pre-edge feature at around 8980 eV, corresponding to the formation of metallic Cu under the CO_2RR (Fig. 6e). As CO_2RR electrolysis went from 0 to 40 min at -0.60 V, the linear combination fitting (LCF) quantitative analysis shows that 50% Cu^{II}Pc was progressively converted to Cu^0 (Supplementary Figure 56b,c). As applied potential increased from -0.60 to -0.81 and -1.14 V, the steady-state relative fraction of metallic Cu further increased from 50 to 69 and 75%, respectively (Fig. 6f). The gradual intensity decay of the edge features at 8985 and 8997 eV suggests that the majority of Cu^{II}Pc catalysts were converted into metallic Cu under CO_2RR conditions (Fig. 6e). *Operando* Fourier-transformed k^3-weighted EXAFS spectra with no phase correction show a decreasing Cu-N feature near 1.3 Å due to the ejection of Cu atoms from CuPc

molecules, and an increasing Cu-Cu feature near 2.2 Å due to formation of metallic Cu clusters (Fig. 6g). EXAFS fitting was used to extract the average Cu-Cu coordination number (CN) by fitting the EXAFS region with correspondingly weighted CuPc and metallic Cu paths based on the quantification of relative fraction of metallic Cu (Figs. 6g, Supplementary Figures 56). At -0.60 V, a very low Cu-Cu CN of around 4.8 indicates the predominance of few-atom Cu clusters given the CN in bulk Cu is 12. At more negative potentials of -0.81 and -1.14 V vs. RHE, the CN increases to 7.8 and 7.6, respectively, indicating the formation of bigger metallic Cu nanograins (Fig. 6h). Simplified geometrical analysis indicates the possible presence of sub-1 nm Cu clusters, such as Cu_4 and Cu_{13} clusters, based on the Cu-Cu CN number of ~5, and 1-2 nm Cu clusters based on the Cu-Cu CN of around 8 (Supplementary Figure 57). It is consistent with previous gas-phase STM studies of CO adsorption on Cu(111) triggering the formation of 0.5 nm $Cu_3(CO)_3$ and 1.5 nm $Cu_{19}(CO)_{13}$ clusters.[19] CO_2RR performance tests reveal that CO is the dominant product with ~70% FE with no detectable C_2H_4 between -0.6 and -1.0 V, and about 2% C_2H_4 FE was achieved at -1.14 V vs. RHE (Supplementary Figure 58). *Operando* HERFD XANES and EXAFS suggest the majority of CuPc evolves into few-nm Cu clusters with an average CN of around 8, which matches well the formation of metallic Cu clusters formed in atomic-scale STEM images (Figs. 6c,d). Given C_2H_4 only forms below -1.0 V, we propose that those metallic Cu clusters with undercoordinated Cu-Cu sites, instead of isolated single Cu atoms in CuPc catalysts, are the true active sites for C-C coupling leading to C_{2+} products, which is consistent with a recent *operando* X-ray study on single-atom Cu-N-C catalysts by Roldan Cuenya et al.[55]

In situ SERS was performed to provide direct molecular evidence of CO-driven ejection of Cu atoms, formation and migration of Cu clusters under CO_2RR-relevant conditions (Figs. 6i-k). An electrochemically deposited roughened Au (EC-Au) substrate was used to enhance Raman signals of adsorbed layer(s) of CuPc molecules (Supplementary Figure 59). *In situ* SERS of CO adsorption on CuPc under different cathodic potentials showed a dominant peak at 1876-1925 cm^{-1} at a mild reducing potential of -0.03 V vs. RHE (Figure 6i), which is consistent with a previous *in situ* IR study of single-atom Cu catalysts with a similar peak at 1895 cm^{-1} under CO_2RR-relevant conditions.[56] Vibrational frequencies of CO-adducts of transition metal porphyrins have also been reported to range from 1943-1980 cm^{-1} when no potentials are applied.[57] Thus, we assign the Raman band at 1876-1925 cm^{-1} to the CO absorbed on the single-atom Cu sites in CuPc (*CO-CuPc). The *CO-CuPc feature exhibits a Stark shift of approximately 70 cm^{-1}/V, indicating that this species is located in the electrochemical double layer (EDL, Supplementary Figure 60).[58] We rule out that this feature is from CO adsorbed on the roughened EC-Au substrate due to the lack of ν(CO) band on this surface in the absence of CuPc molecules (Supplementary Figure 61). A weak and broad vibrational band from 2035 to 2065 cm^{-1} developed at a more negative potential of -0.33 to -0.53 V, which was assigned to *CO on few-nm Cu clusters.[54] This feature does not persist at more cathodic potentials and is only sporadically observed, which is possibly due to the small amount of metastable Cu clusters in the initial stage of CO-driven ejection of Cu atoms from CuPc catalysts. A CO_2RR-relevant potential of -0.93 V vs. RHE was applied to simulate the electrochemical conditions for triggering the ejection of Cu atoms from CuPc catalysts (Fig. 6j). Following an extended potential hold time of 30 min, the *CO-CuPc feature has disappeared, indicating the majority of CuPc evolving into Cu clusters and is now replaced by a strong Raman peak ranging from 2025 to 2100 cm^{-1}, which was deconvoluted into a high-frequency band (HFB) centered at 2095 cm^{-1} and a low-frequency band (LFB) at <2075 cm^{-1} at a mild potential of -0.33 V (Fig. 6j). The frequency of the LFB and HFB match closely with CO adsorption on the terrace and isolated step/defect sites, respectively.[59-61] At potentials from -0.53 V to -0.93 V, the HFB

intensity decreased markedly, and the only dominant feature is the LFB after -0.83 V. The evolution from Cu step to terrace sites is consistent with the continuous growth of few-nm Cu clusters into larger Cu nanograins with decaying contributions of surface step/defect sites (Fig. 6a). After an additional potential hold of 30 min at -0.93 V, the HFB is no longer observable even at mild reduction potentials (Fig. 6k). The *in situ* SERS spectra with a broad band at 2000-2100 cm^{-1} resemble those typically observed for Cu nanocatalysts or bulk Cu electrodes (Supplementary Figure 52, Supplementary Table 5). In summary, *in situ* SERS results suggest that CO triggers the ejection of single-atom Cu in CuPc catalysts and subsequent formation and migration of few-nm clusters. Those Cu clusters experience continuous CO-driven reconstruction from small Cu clusters with more stepped structures to larger Cu nanograins with more terrace-like and less rough structures.

The combination of atomic-scale STEM images, *operando* X-ray spectroscopy and *in situ* Raman spectroscopy provides comprehensive structural and molecular pictures of the evolution mechanism of Cu nanocatalysts: the structural picture of how Cu atoms and more importantly, the molecular driving force regarding why Cu atoms move under CO_2RR. CO intermediates eject single-atom Cu and trigger the formation of few-nm metallic Cu clusters followed by their migration and evolution into larger Cu nanograins. Based on extensive *ex situ* SEM imaging analysis (Supplementary Figures 46-49, Supplementary Table 4), the absence of CO significantly slows down Cu migration while the addition of CO notably accelerates Cu migration. The remaining question is whether CO-driven migration of cooper carbonyl species occurs on electrode surfaces or in the solution phase.

Distinguishing surface from solution migration mechanisms

We designed a control experiment where two negatively polarized working electrodes (WE) are used simultaneously in proximity (Supplementary Figure 62). The Cu nanocube catalysts are deposited on only one of them, while the other electrode is a blank carbon paper substrate as the control electrode for detecting possible solution-mediated Cu migration. After 5 hours at -1.0 V vs. RHE in the absence/presence of CO_2, the surface morphology of the clean electrode was investigated by SEM (Supplementary Figure 63). In Ar-saturated 0.1 M $KHCO_3$, where only the HER can take place, the previously clean electrode is now evenly covered with large numbers of small Cu nanoparticles. In stark contrast, the second electrode remains nearly clean in CO_2-saturated 0.1 M $KHCO_3$, where the CO_2RR takes place. Under the HER conditions, cathodic corrosion is likely taking place, which leads to the dissolution of Cu species into the solution and is known to lead to the nucleation of new nanoparticles at adjacent locations.[47,62,63] During the CO_2RR, a different mechanism leads to catalyst reconstruction in which the migration of copper carbonyl species is confined to the electrode surface while Cu migration through a solution-mediated mechanism remains nearly undetectable. A similar observation was recently reported by Buonsanti et al.:[35] During CO_2RR, online ICP-MS detected barely any Cu in solution at potentials down to -1.1V vs RHE, which as ascribed to rapid redeposition of any mobile species at these potentials. We previously showed that during the CO_2RR, large amounts of CO reservoirs are formed near the surface with as many as 100 molecules of CO per surface Cu atom.[64] This study indicates that CO achieves a maximum coverage on Cu surfaces under the CO_2RR, which is later supported by the strong effect of CO coverage on Cu ejection rate in DFT simulations. Extensive reconstruction is expected under such conditions, as corroborated with gas-phase STM evidence of CO-driven Cu reconstruction[19] and detection of undercoordinated copper by *in situ* generated

CO using IR spectroscopy.[60] In summary, *ex situ* SEM experiments suggest that surface migration mechanisms of copper carbonyls are predominant in comparison to solution-mediated mechanisms.

DFT simulations with atomic insights into copper carbonyl

To develop an atomic-scale understanding of the CO-driven migration of Cu atoms on Cu nanocubes, we performed DFT calculations (for computational details see SI). Xu et al. developed a DFT-based framework and successfully described the formation of sub-nanometer Cu clusters on Cu(111) in the presence of CO[20]. They demonstrated that CO could facilitate the migration of Cu atoms by decreasing the activation energy barrier for the ejection of Cu atoms from step/kink sites to form adatoms on adjacent Cu terraces. For all CO coverages studied, this Cu atom ejection step was shown to be the rate-limiting step for the entire Cu cluster formation process. In a subsequent study, they also showed that at the dilute CO-coverage limit, CO-induced Cu adatom formation is easier on Cu(100) when the source of the ejected Cu atoms is the step edge of the Cu(511) surface, as opposed to Cu(100).[65] Accordingly, here we studied the ejection of Cu atoms from a Cu(511) surface, a stepped surface with Cu(100) terraces intended to represent the edge of a Cu nanocube exposing Cu(100) facets, and we evaluated the Cu atom ejection kinetics as a function of CO coverage. The influence of CO on the ejection of Cu atoms was considered from vacuum conditions, i.e., no CO present, up to 6/9 monolayer (ML) coverage of CO on Cu(511). 6/9 ML is the maximum CO coverage we considered for the Cu atom ejection study. At any CO coverage beyond 6/9 ML, the most stable adsorption configuration involves at least one CO molecule in a physisorbed state. Such a physisorbed CO molecule is located at least 5.7 Å from the Cu(511) surface and has practically no interaction with the Cu surface. For each CO coverage, we evaluated all possible CO adsorption configurations with each CO molecule occupying different combinations of adsorption sites on Cu(511) and identified the most stable overlayer structure (Supplementary Figure 64).

The most stable CO overlayer structure for each CO-coverage studied was used as the initial state for the Cu-atom ejection. For each initial state, several possible final states were examined in which a surface Cu atom with or without an attached CO molecule, depending on the CO coverage, was displaced from its initial position to a landing site on the adjacent terrace of Cu(511). Next, all ejection pathways were explored for all combinations of initial and final states. Figs. 7a-g shows the initial, transition and final state for the minimum energy path calculated for each CO-coverage studied. In all cases explored, the energetically preferred ejection path involved the displacement of a Cu atom from the step to the terrace of Cu(511), with the displaced Cu atom being decorated with a single CO molecule. Final states with more than one CO molecule adsorbed on the ejected Cu atom were much less stable. The highest activation energy barrier for the Cu atom ejection step was determined under vacuum (E_b = 1.0 eV). With increasing CO coverage, E_b decreases. The decrease in activation energy is not a monotonic function of CO coverage. As shown in Fig. 7h, for CO-coverages between 1/9-4/9 ML, when the step-edge Cu atoms on Cu(511) (green spheres in Fig. 7a-g) are partially covered by CO, the barrier is ~0.7 eV. For higher CO-coverages (5/9-6/9 ML), when the Cu(511) step-edge atoms are fully covered by CO (one CO adsorbed per step-edge Cu atom), the barrier drops further to ~0.4 eV. The energetics of the respective activation energy barrier (E_b) and the final state for the Cu adatom formation process on Cu(511) as a function of CO coverage is shown in Supplementary Figure 65. Clearly, the presence of CO accelerates Cu atom ejection from the Cu(511) step edge. Assuming the standard pre-exponential factor of 10^{13} s^{-1}, and at room temperature, we would expect approximately one Cu atom ejection event per second for CO-coverages between 1/9-4/9 ML, and about six orders of magnitude more ejection events

per second when CO-coverage reaches 5/9-6/9 ML. Our DFT model with the maximum coverage of 6/9 ML effectively represents a Cu catalyst surface saturated with CO, which is consistent with our previous experimental observation from on-stream substitution of reactant isotope (OSRI) under CO_2RR conditions.[64] Our later DFT calculations also indicate that the CO stretch features on various extended Cu facets and Cu cluster sites can vary within a range of ~30 cm^{-1} (Supplementary Tables 6-7). Considering both our DFT simulations and *in situ* Raman of Cu nanocatalysts (Supplementary Figure 52), we hypothesize that the spectroscopic signature of copper carbonyl species (*CO on few-nm Cu clusters and larger Cu nanograins) lies in a similar spectrum window (2000-2100 cm^{-1}) to that of *CO on extended Cu surfaces. Overall, our results point to the importance of CO, a key intermediate generated during CO_2RR, for accelerating the ejection of step-edge Cu atoms and migration of copper carbonyl species, leading to the dynamic evolution of Cu nanocubes and CuPc single-atom catalysts as observed in our experiments.

Although the exact nature of copper carbonyl species is still under debate and warrants more direct experimental observations, we propose a general chemical formula, $[Cu_x(CO)_y]^z$, where x and y represent the number of Cu atoms and CO molecules, and z represent the total charge. Early work on low-temperature gas-phase vibrational spectroscopy suggested the formation of $[Cu(CO)_y]$ where y = 1, 2, or 3, or a dimeric Cu hexacarbonyl, $[Cu_2(CO)_6]$[32,33]. From early gas-phase STM studies of CO adsorption on Cu(111), chemical formulas of $Cu_3(CO)_3$ and $Cu_{19}(CO)_{13}$ were proposed as the most stable configurations of CO-adsorbed Cu clusters[18,19]. Our *operando* EC-STEM and X-ray studies provide compelling evidence that pristine Cu@Cu_2O nanocubes evolve into metallic Cu nanograins. *In situ* SERS and DFT simulations reveal CO-driven ejection of single-atom Cu and migration of few-nm metallic Cu clusters on the electrode surface, indicating the presence of neutral copper carbonyl species during the entire course of the dynamic evolution process under CO_2RR conditions. Since our DFT calculations indicate that final states with more than one CO molecule adsorbed on each ejected Cu atom are much less stable, we propose that neutral copper carbonyl, [Cu(CO)], species are highly mobile on electrified catalyst surfaces where they drive dynamic migration of highly mobile subnanometer Cu clusters on catalyst surfaces.

Conclusion

This study employs multimodal *operando* EC-STEM and synchrotron-based hard XAS and resonant soft X-ray scattering to track the dynamic evolution of Cu nanocubes as a model system of practical nanocatalysts for the CO_2RR. *Operando* electrochemical 4D-STEM, based on in-depth machine learning analysis, emerges as a powerful method to quantify the relative degree of crystallinity of polycrystalline active sites and provide unique insights into the complex structure of metallic Cu nanograins. *In situ* Raman and DFT calculations, supported by extensive *ex situ* SEM observations, reveal that absorbed CO molecules drive the formation of copper carbonyl species and accelerate the migration of Cu atoms on catalyst surfaces. The mobility of copper carbonyl species, [Cu(CO)], strongly depends on the electrolyte environment and/or external electrical fields. We anticipate that molecular-level surface-sensitive *operando* methods have the potential to provide more compelling evidence of the exact nature of copper carbonyl among other intermediate species. This study shows that multimodal *operando* methods, with atomic-level theoretical simulations, serve as a powerful toolbox to advance our structural and molecular understanding of the dynamic evolution of electrocatalysts and nature of active sites for CO_2 reduction and, by extension, the broader landscape of energy-related electrochemical reactions.

Methods

Synthesis: Copper nanocubes with different sizes were synthesized via a colloidal method using the chemicals in Supplementary Table 1. Trioctylamine and Trioctylphosphine oxide were sealed in a 50 mL three neck round bottom flask and degassed under vacuum using a Schlenk line. The solution was heated to 80 °C under vacuum. The solution was further degassed by alternatingly applying vacuum for 4 minutes and flowing Argon for 1 minute for a total of 3 times. Then, CuBr was added under Argon flow and the solution degassed for another 5 minutes. For 27 nm cubes, the reaction mixture was heated to 250 °C and kept there for 30 minutes. For 55 nm cubes, the solution was instead heated to 280 °C and kept there for 1 hour. The solution was then allowed to cool to 80 °C, after which the nanocubes were collected by centrifugation (12,000 rpm, 19,520 g, 10 min). The cubes were washed twice with hexanes and finally redispersed in hexane. The concentration was determined by inductively coupled plasma optical emission spectroscopy (ICP-OES) on a Perkin Elmer ICP Optima 7000 DV Spectrometer.

CO_2RR performance tests in H-cell and MEA: H-cell performance tests were conducted in an H-cell with catalyst-coated carbon paper (Sigracet 39AA) as the working electrode, a platinum mesh counter electrode and a 3M Ag/AgCl reference electrode (WPI DRI-REF 2 mm). The catalyst loading was 100 μg cm^{-2}, and the surface area of the electrode was typically 0.5 cm^2. The electrolyte was CO_2-saturated $KHCO_3$ (0.1 M, pH 6.8), and the solution was continuously purged with CO_2 (20 sccm) during the tests. Gas products were quantified using a gas chromatograph (Agilent 7890B). Liquid products were quantified *via* nuclear magnetic resonance (Bruker AV600) using a water suppression technique. For MEA tests, the cathode was prepared by spray-coating carbon black and as-prepared Cu Cube 55 nm onto carbon paper (AvCarb GDS5130). 1 mg of Carbon black (Vulcan XC 72) was dispersed in a mixture of 2-propanol and Nafion solution. The carbon black ink was spray-coated on the carbon paper with a loading of ~0.1 mg/cm^2 and Cu Cube 55 nm ink was spray-coated with a loading of ~0.1 mg/cm^2. The oxygen evolution reaction catalyst is titanium foam-supported iridium oxide (Magneto). The cathode and anode is separated by the anion exchange membrane (Sustainion® X37-50 grade 60 Membrane). The anolyte is 0.1 M $KHCO_3$ and it was circulated using a peristaltic pump. Humidified CO_2 gas was fed at 15 sccm/cm^2. Electrolysis was maintained for at least 30 min prior to collecting gas and liquid samples.

***Operando* EC- and 4D-STEM and *ex situ* STEM-EELS**: A Protochips Poseidon liquid-cell holder and Gamry potentiostatic were used for electrochemical measurements in EC-STEM. The electrochemical chip encapsulates a liquid pocket within two electron-transparent SiN_x windows, which can withstand the ultrahigh vacuum (10^{-8} Torr) inside the TEM chamber. 2 μL of 0.1 mg/mL Cu NPs solution was drop cast on the microchip and dried to evaporate residual hexane in a vacuum pump. *Operando* EC-STEM imaging was performed in CO_2-saturated 0.1 M $KHCO_3$ with a spacer of ~500 nm in a Tecnai F-20 STEM. The electrochemical potential of Pt pseudo-RE was calibrated to be around 0.8 ± 0.1 V vs. RHE based on our previous studies.[8] A LSV scan from 0.4 to around 0 V was applied to trigger a hydrogen bubble, which enables a significantly thinner (~100 nm) yet electrochemically accessible liquid film. *Operando* EC-STEM image was acquired at a beam current of ~4 pA and a speed of 4 s/frame (1024×1024 pixels with a dwell time of 3.2

μs/pixel). A beam dose was calculated to be ~80 e^-/nm^2 per frame (dose rate of ~20 e^-/nm^2s) for a field of view (FOV) of ~1,000 nm. Beam dose control experiments were routinely performed before each dynamic videos with a similar amount of time as following electrochemical reaction time to ensure no evidence of beam damage. 4D-STEM experiments were performed using an electron microscope pixel array detector (EMPAD) in a scanning nanobeam electron diffraction mode with a probe size of ~1.3 nm in the full-width at half-maximum, 256×256 scan over an area of ~1000×1000 nm^2. The total dose for one 4D-STEM data was calculated to be ~2,000 e/nm^2 at a beam current of ~1 pA for an exposure time of 5 ms/pixel (4 ms per pixel acquisition time and 1 ms/pixel readout time). *Ex situ* atomic-scale HAADF-STEM imaging and EELS were performed in a fifth-order aberration-corrected STEM (Titan) operated at 300 keV with a beam convergence semi-angle of 30 mrad. EELS spectral images were acquired with a 0.25 eV/channel energy dispersion (energy resolution, 0.75 eV) in a Gatan spectrometer with a size of 100~200 pixels and an acquisition time of 10-20 ms per pixel. The Cu and O elemental maps were extracted using Cu $L_{3,2}$ and O K edges from EELS spectrum images and processed using principal component analysis (PCA, 3 components) and the linear combination of power law (LCPL) to subtract the background in ImageJ software.

***Operando* HERFD XAS measurements**: Cu K-edge XANES and EXAFS were acquired under HERFD mode at the PIPOXS beamline of the Cornell High Energy Synchrotron Source (CHESS under ring conditions of 100 mA at 6 GeV. Beam was provided by a cryogenically-cooled Si(311) monochromator. A pair of Rh-coated focusing mirrors were used to focus the beam to a spot of 120 × 400 μm. The intensity before the sample was monitored using N_2-filled ion chambers and the energy was calibrated based on the characteristic absorption edge of Cu metal foil at 8979.0 eV. Fluorescence from the copper was energy selected using five spherically-bent Si(444) analyzer crystals (R = 850 mm) arranged in Rowland geometry together with a Pilatus 100K detector; the space between the samples, analyzers, and detector was filled with helium gas to minimize attenuation of the fluorescence signal. Fourier transformed EXAFS spectra, based on the ATHENA software package, were plotted by applying a Hanning window from 3 to 10 $Å^{-1}$ with k^2-weighting and no phase correction. The HERFD XAS uses one particular fluorescence decay channel, Cu $K\alpha_1$ emission line at 8048 eV to enable a higher energy resolution of ~0.66 eV, when compared to 1.6 eV for conventional XAS.[9] The design of customized cell can be found in our previous reports.[9] The working electrode (WE) of Cu cubes deposited on carbon paper was immersed in CO_2-saturated 0.1 M $KHCO_3$. A carbon rod as the counter electrode (CE) was placed 3 cm away from the WE to avoid possible interference of electrochemical reactions on the WE. The reference electrode (Ag/AgCl (sat. KCl)) was placed (via a salt bridge) at the bottom of the cell to minimize the iR drop during electrochemical testing. All three electrodes were connected to a potentiostat (Biologic SP-200) during *operando* X-ray data acquisition.

***Operando* electrochemical resonant soft X-ray scattering (EC-RSoXS) measurements:** SAXS measurements were performed with a liquid thickness of around 1 μm in a customized liquid-cell holder with the same design as the *operando* EC-STEM holder. SAXS data were collected at the Advanced Light Source (ALS) beamline 11.0.1.2 with a back-illuminated Princeton PI-MTE CCD

cooled to −45 °C. Scattering patterns of Cu nanocubes were collected for 0.6 s to minimize soft X-ray beam damage. RSoXS data fitting was conducted using software package Scatter.[66]

4D-STEM hierarchical clustering: Hierarchical clustering is used to segment the complex 4D dataset and provide a better visualization of different local structures.[49] In this method, each diffraction pattern in the 4D-STEM dataset was treated as a data point. We first corrected the drift of the diffraction pattern induced by the misaligned beam tilt during the scanning through the center of mass of the center disk. Then we added a ring mask to remove the noise pixel at the edge of the diffraction pattern. After these preprocessing, we used a dimension reduction method called uniform manifold approximation and projection (UMAP)[67] to embed the diffraction into a three-dimensional (3D) manifold space. We applied the K-means clustering method hierarchically and the whole 4D dataset was separated into several clusters based on the similarity of the data points.[68] The clustering labels were mapped back to real space to visualize the segmentation (**Figs. 3b, e**), and the mean diffraction patterns of the cluster are generated and plotted in log scale **(Figs. 3c, f)**, which represent the averaged feature of the corresponding clusters.

Fluctuation electron microscopy (FEM) analysis: The FEM method[51] was used to identify the crystallinity level of the materials based on the fluctuation of the middle range order in the diffraction. The maximum diffraction was first generated to determine the radius of the diffraction spots. Since Cu has the face-centered cubic (fcc) lattice, the first four orders with strong intensity are {111}, {200}, {220} and {311}. To reduce the sample tilting effect, we use ring masks to cover (i) {111} and {200}, (ii) {220} and {311} separately and normalized variance in the rings are calculated. The liquid background region identified from the clustering method was set as zero. The final FEM map is the summation of the two images.

***In Situ* Surface-Enhanced Raman Spectroscopy (SERS):** A 300 nm gold film was deposited onto a PTFE filter membrane using a CHA SE-600 Electron Beam Evaporator (CHA Industries, USA) equipped with a cryopump. Electrochemical deposition of Au onto the Au film (EC-Au) was performed in a pH of 6 solution containing 0.01 M of gold (III) chloride ($AuCl_3$, Sigma, 99%) and 0.1 M potassium chloride (KCl, Fisher Chemical, P217-3). Trifluoro acetic acid (TFA, TCI America, T0431) was used to dissolve CuPc (Sigma, 99%) at 1.72 mM concentration. The EC-Au sample was incubated in the CuPc/TFA solution for 55 minutes under room temperature, followed by washing with TFA solvent and Type 1 water. The sample was placed in an *in situ* SERS cell and used as the WE. A single junction Ag/AgCl reference electrode was used (CHI111, CHI instruments), and the counter electrode was a Pt wire. A continuous flow of CO at 40 sccm was supplied to the back backside of the EC-Au sample. The electrolyte used was either a 0.5 M potassium sulfate solution at pH 4 (K_2SO_4, Fisher Chemicals, P304-500) or 0.1 M potassium bicarbonate solution ($KHCO_3$, Thermo Scientific, A122429.36). The excitation laser used was 633 nm at 0.42 mW power. Spectra acquisition was performed with 5-second exposure and 10 accumulations.

Computational details: Total energies and optimized structures of the different models were obtained from periodic density functional theory (DFT) calculations carried out using the Vienna Ab Initio Simulation Package (VASP).[69,70] The exchange correlation contribution to the total

energy was computed using the Perdew-Burke-Ernzerhof (PBE) exchange-correlation functional within the generalized gradient approximation (GGA).[71] The Kohn-Sham equations were solved with a plane-wave basis set with an energy cutoff of 400 eV. The effect of core electrons on the valence region was described by the projected augmented wave (PAW) method as implemented in VASP.[72] The Cu(511) surface was modelled using a 1×3 supercell with 12 atomic layers. The (511) facet is a high-index vicinal stepped surface which is characterized by the [3(100)×(111)] structure with three-atom-row wide (100) terraces separated by one-atom-row wide (111) step edges. This surface offers an atomistic model with computationally viable unit cell size while properly capturing the structure of step defects adjacent to the (100) facets. Importantly, (100) is the surface facet that dominates the experimental Cu nanocube catalyst. We have recently adopted the (511) slab model for a wide range of metals with face-centered-cubic bulk structures and properly captured the atom ejection process from step edges adjacent to the (100) facets of these metals.[65]

During energy optimization, the six bottommost layers were frozen at their bulk-truncated positions, and the six topmost layers were fully relaxed. Structural optimization was ensured by converging forces acting on atoms to below 0.01 $eV \cdot Å^{-1}$. The numerical integration was carried out in the reciprocal space using a 4 × 4 × 1 k point grid centered at the Gamma point.[73] All models include 20 Å of vacuum between successive slabs in the Z direction. Adsorption was allowed on only one side of the metal slab, and the electrostatic potential was adjusted accordingly.[74,75] The optimized lattice constant for bulk Cu is 3.638 Å, in good agreement with the experimental value of 3.678 Å.[76] All transition state (TS) structures were determined using the climbing-image nudged-elastic-band (CI-NEB) method employing 5 intermediate images.[77] All TS structures were further characterized by vibrational frequency analysis through Hessian matrix diagonalization, where the matrix elements were obtained by finite differences of analytical gradients with displacements of 0.015 Å. The PBE exchange-correlation functional alone accurately captures the bulk cohesive energy of Cu (3.48 eV; in excellent agreement with the experimental value of 3.49 eV), while the addition of van der Waals (vdW) corrections leads to overestimation of this value (Supplementary Table 6). Since an accurate description of the metal-metal interaction is essential for modeling the energetics of surface atom ejection, we applied the PBE functional without any further vdW corrections throughout this work.

Data availability:
All electronic structures files in DFT simulations are available in supplementary files. Raw EC-STEM movie datasets are available in supplementary videos. Given the terabyte-level sizes of all EC-STEM images and 4D-STEM datasets, all relevant TEM data are available from the corresponding author on request.

Code availability:
Codes and algorithms used in this study are available in the Methods section and can be found in previous studies in corresponding references. No new codes or algorithms are developed in this study. Further requests of codes can be directed to the corresponding author.

Acknowledgement:
This work was supported by the Director, Office of Science, Office of Basic Energy Sciences, Chemical Sciences, Geosciences, & Biosciences Division, of the US Department of Energy under

Contract DE-AC02-05CH11231, FWP CH030201 (Catalysis Research Program). *Operando* EC-STEM work was supported by the Center for Alkaline-Based Energy Solutions (CABES), an Energy Frontier Research Center (EFRC) program supported by the U.S. Department of Energy, under grant DE-SC0019445. This work used TEM facilities at the Molecular Foundry was supported by the Office of Science, Office of Basic Energy Sciences, of the U.S. Department of Energy under Contract No. DE-AC02-05CH11231. This research used the beamline 11.0.1.2 of the Advanced Light Source, which is a DOE Office of Science User Facility under contract no. DE-AC02-05CH11231. This work made use of TEM facilities at the CCMR which are supported through the National Science Foundation Materials Research Science and Engineering Center (NSF MRSEC) program (DMR-1719875). This work is based on research conducted at the Center for High-Energy X-ray Sciences (CHEXS), which is supported by the National Science Foundation (BIO, ENG and MPS Directorates) under award DMR-1829070. Y.H. and C.S. are supported by NSF CAREER (CMMI–2239545) and Welch Foundation (C-2065). We thank H. Celik and UC Berkeley's NMR facility at the College of Chemistry (CoC-NMR), which is supported in part by NIH S10OD024998. Work at UW-Madison was supported by the U.S. Department of Energy, Basic Energy Sciences (DOE-BES), Division of Chemical Sciences, Catalysis Science Program, Grant DE-FG02-05ER15731. We used resources at the National Energy Research Scientific Computing Center, a DOE Office of Science User Facility supported by the Office of Science of the U.S. Department of Energy under Contract No. DE-AC02-05CH11231 using NERSC award BES-ERCAP0027367. C.C. and J.J. gratefully acknowledge support from Suzhou Industrial Park Scholarships. Y.Y. acknowledges the generous support from the Miller Research Fellowship. Y.Y. acknowledges the generous support from the Kavli Institute at Cornell (KIC) Instrumentation Grant and the Fast Grant from Cornell Atkinson Center for Sustainability and the 2030 Project: A Cornell Climate Initiative.

Author contributions

†Y.Y., J.F., M.F.V. and C.C. contributed equally. Y.Y., J.F. and C.C. initiated the project under the guidance of P.Y. Y.Y. performed atomic-scale STEM-EELS and *operando* EC- and 4D-STEM measurements. Y.Y. and J.F. performed HERFD XAS measurements of Cu nanocatalysts with the help of C.J.P.. J.F. performed all electrochemical measurements and performance tests in H-cells. J.F. performed *operando* XAS analysis of CuPc catalysts with the help of M.F.G., Y.S., and N.E.S. C.C., Y.Y. and J.F. synthesized Cu nanocubes. M.F.V performed DFT simulations with the help of M.R. and L.X. under the guidance of M.M. C.S. performed machine learning based 4D-STEM clustering under the guidance of Y.H. M.F.G. performed *in situ* Raman of Cu nanocatalysts under the guidance of P.Y. Y.M.M. and P.J. performed *in situ* SERS studies of single-atom CuPc catalysts and corresponding analysis under the guidance of Z.C. S.L. performed atomic-scale STEM imaging analysis under the guidance of Y.Y. Z.P. performed RSoXS analysis under the guidance of C.W. G.L. performed MEA measurements under the guidance of P.Y. J.J. prepared the schematic in Figure 1. Y.S. performed SEM measurements. M.B.S and V.B.M. contributed to discussions on Cu migration mechanisms. All authors wrote, revised and approved the manuscript.

Competing interests:

The authors declare no competing financial interest.

Additional Information:

Supplementary Figures 1-65; Supplementary Tables 1-7; Supplementary References; Supplementary Videos 1-5; Captions for supplementary electronic files of DFT optimized structures; Captions for supplementary Videos 1-5

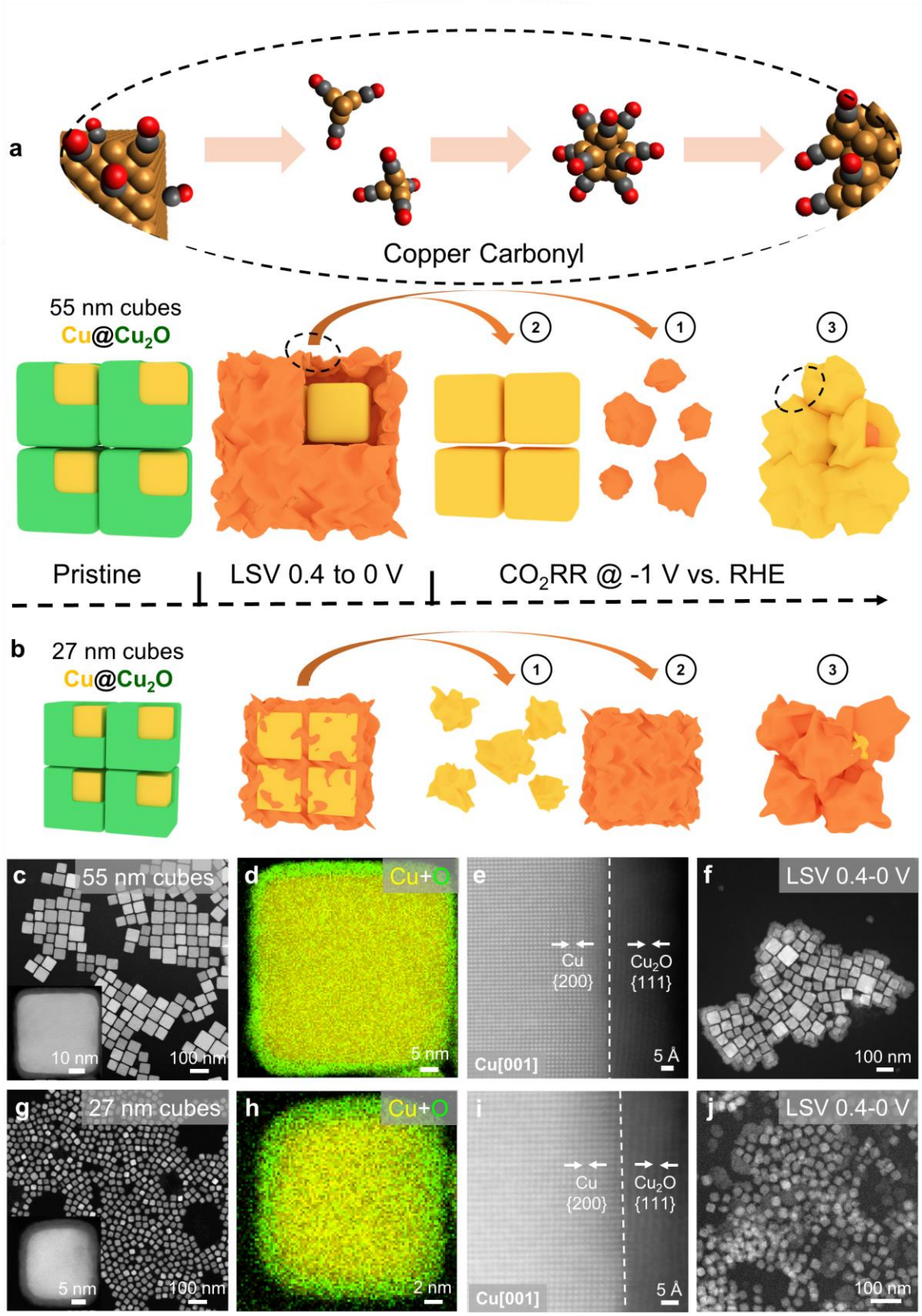

Figure 1. Overview of the dynamic evolution of Cu@Cu_2O nanocubes to metallic poly-Cu nanograins a, Schematic of Cu carbonyl driven restructuring of 55 nm Cu@Cu_2O nanocubes.

They experienced the formation of a spongy Cu shell at the perimeter of the cubic core after an initial LSV scan from 0.4 to 0 V vs. RHE. During the CO_2RR, Cu nanocubes experience complete transformation to polycrystalline Cu nanograins (step 3) starting with the spongy Cu shell (step 1) followed by the cubic Cu core (step 2). The section in the dashed ellipse corresponds to the ejection of single-atom Cu and migration of few-nm Cu clusters during dynamic evolution of Cu nanocatalysts. **b**, 27 nm nanocubes experienced a similar transformation to polycrystalline Cu nanograins but in the reverse order starting with the smaller, and more reactive, cubic Cu core followed by the spongy Cu shell. **c-e** and **g-h**, HAADF-STEM images and EELS elemental maps of 55 and 27 nm $Cu@Cu_2O$ nanocubes, respectively, with a single-crystal metallic Cu core surrounded by a ~2 nm Cu_2O shell. **f, j,** *Operando* EC-STEM images of 55 and 27 nm nanocubes, respectively, with the formation of spongy Cu shell after the LSV from 0.4 to around 0 V.

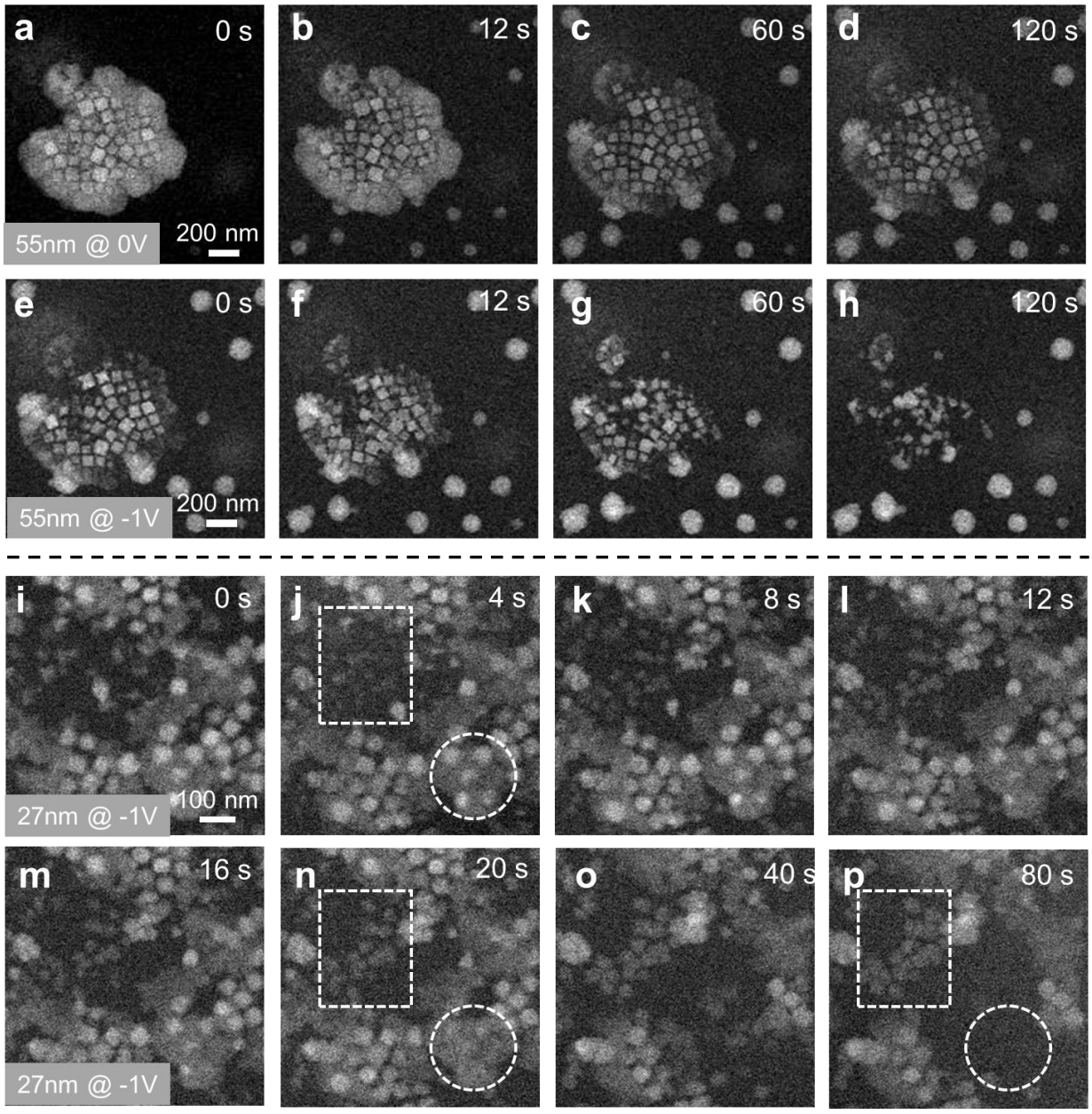

Figure 2. *Operando* EC-STEM images of 55 and 27 nm Cu nanocubes under CO_2RR a-d and **e-h** Dynamic evolution of 55 nm nanocubes under chronoamperometry (CA) showing the transformation of the Cu spongy shell to spherical poly-Cu nanograins at a mild potential of 0 V. (**a-d**) and subsequent evolution of the cubic Cu core to poly-Cu nanograins under the CO_2RR condition at -1 V. (**e-h**). **i-p**, Dynamic evolution of 27 nm cubes at -1 V showing the transformation of the cubic Cu core (**j** vs. **n**) followed by the spongy Cu shell.

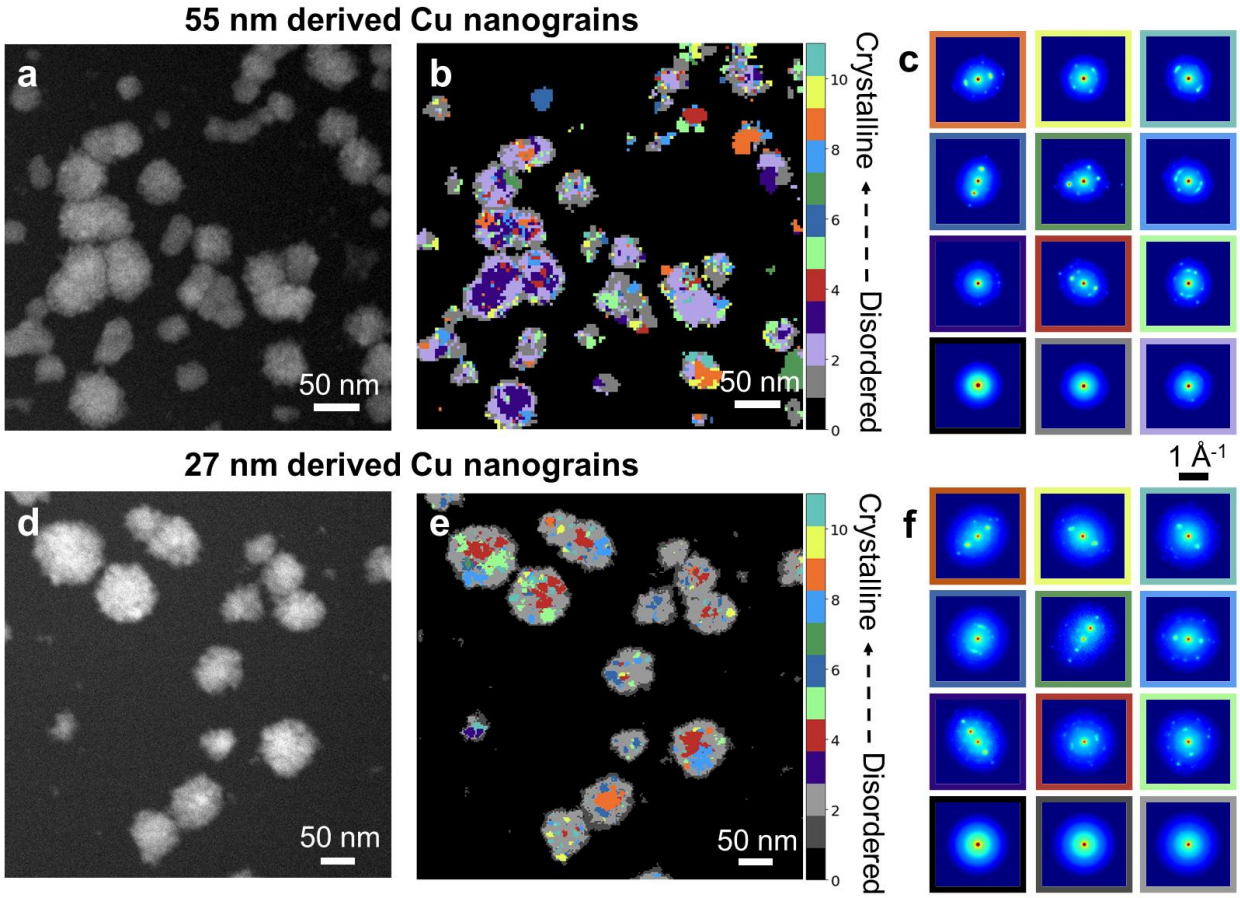

Figure 3. Machine-learning-assisted *operando* electrochemical 4D-STEM structural analysis (a-b, d-e) *Operando* HAADF-STEM images and 4D-STEM clustering analysis of 55 and 27 nm nanocube-derived Cu nanograins at -1 V. (**b**) The false-color 4D-STEM map shows that the majority of 55 nm nanocube-derived nanograins are mainly polycrystalline Cu with various colors. (**c**) Corresponding diffraction patterns with different border colors representing different crystalline orientations. The number 0 is the amorphous liquid/SiN_x background and the number of 1 in grey represents more disordered/amorphous Cu domains. The rest of numbers of 2 to 11 in various colors represent more crystalline Cu domains. The dashed arrow in between (b) and (c) shows the transition from disordered/amorphous to ordered domains. **e-f**, In contrast, 27 nm nanocube-derived nanograins have a significant portion of Cu nanograins that are nearly amorphous/disordered as shown by the diffraction patterns in deep and light grey.

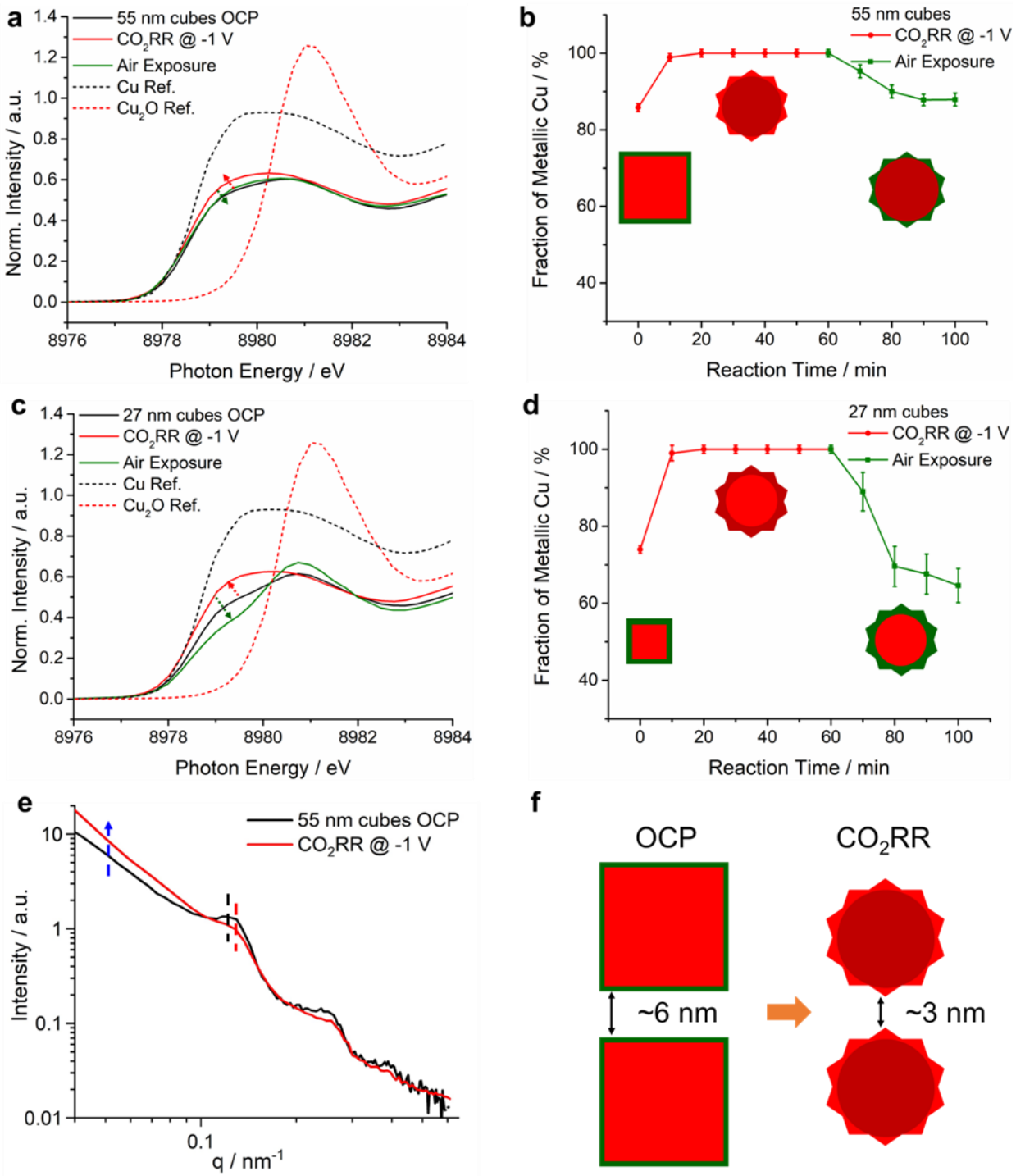

Figure 4. ***Operando*** **hard X-ray spectroscopy and soft X-ray scattering. a, c,** *Operando* HERFD XANES spectra of 55 and 27 nm nanocubes at the open circuit potential (OCP), under steady-state CO_2RR at -1 V and after 1 h following post-electrolysis air exposure, along with the standard references. Norm. means normalized. The red and green arrows correspond to electroreduction and reoxidation, respectively. **b, d,** Corresponding quantitative analysis of the relative fraction of metallic Cu from the linear combination fitting (LCF), showing the conversion from 55 and 27 nm $Cu@Cu_2O$ nanocubes, respectively, to fully metallic Cu nanograins followed

by subsequent partial oxidation of surface Cu. The error bars represent the uncertainty of the LCF fit. **e, f,** *Operando* EC-RSoXS spectra and corresponding structural models showing particle aggregation with a decay of the average particle-particle distances from 5.8 ± 1.6 nm at the OCP to 2.7 ± 1.8 nm under CO_2RR at -1 V. The error bars are from RSoXS fitting results. The blue arrow marks the increase in scattering intensity and the change from the black to red dashed line corresponds to a higher q value of the first maximum peak, suggesting significant aggregation under the CO_2RR.

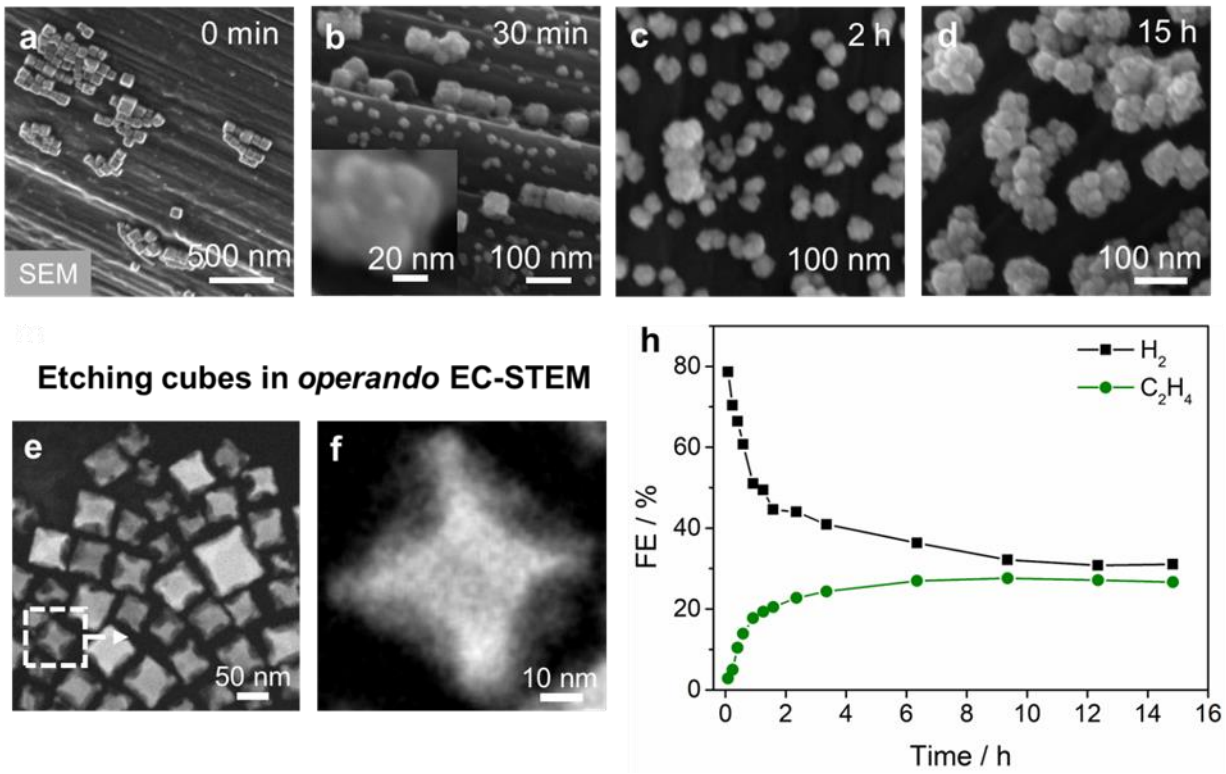

Figure 5. Evidence for CO-driven evolution of Cu nanocubes in benchtop experiments. a-d, *Ex situ* SEM images of 55 nm cubes loaded on carbon paper performed in an H-cell at -1 V in CO_2-saturated 0.1 M $KHCO_3$, showing a similar evolution from nanocubes to polycrystalline nanograins. The inset with dashed border in (**b**) is a Cu cube with partially etched edges in H-cell, which is similar to the etched cube in the dashed box in (**e**). **e-f,** *Operando* EC-STEM images of structural evolution of 55 nm Cu cubic core showing a similar edge etching feature to that in *ex situ* SEM image in (**b**). (**g**) H-cell CO_2RR performance of Faradaic efficiency (FE) of H_2 and C_2H_4 of 55 nm nanocubes at -1 V reaching a steady state after ~2 h and maintaining performance for 15 h.

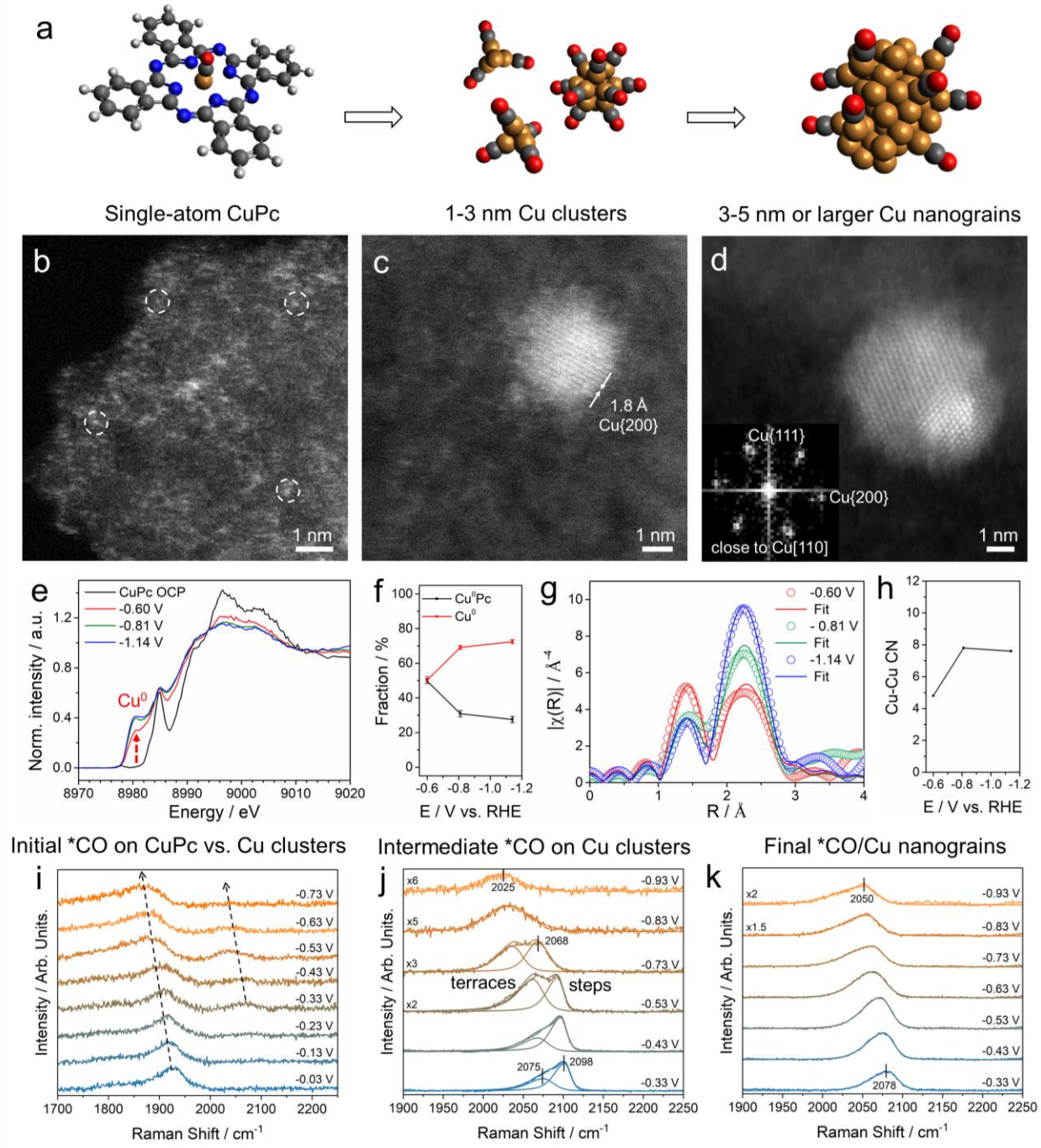

Figure 6 Evidence of CO-driven migration of Cu in single atom model system. (a) Schematic illustrating the CO-driven formation of Cu clusters from a model single-atom CuPc catalysts and migration into larger Cu nanograins. Yellow, red, grey and silver balls represent Cu, O, C and H atoms, respectively. (b-d) Selective atomic-scale HAADF-STEM images of pristine single-atom CuPc catalysts with some Cu atoms highlighted in the dashed circles (b) 1-3 nm Cu clusters (c) and 3-5 nm or larger Cu nanograins with one Cu nanoparticle close to the Cu[110] zone axis (d). (e-f) *Operando* HERFD XANES showing about 75% $Cu^{II}Pc$ evolved into metallic Cu^0 nanograins at -1.1 V vs. RHE. The error bars represent the uncertainty of the LCF fit. (g-h) *Operando* EXAFS showing an estimated Cu-Cu CN of around 5 to 8 corresponding to undercoordinated Cu clusters.

(i) *Operando* surfaced enhanced Raman spectroscopy (SERS) showing the *CO adsorption on single-atom CuPc (~1900 cm^{-1}) followed by the formation of *CO on Cu clusters (~2100 cm^{-1}) during the initial stage of the CO_2RR. (j) *Operando* SERS showing the *CO adsorption on terraces (~2050 cm^{-1}) and steps (~2100 cm^{-1}) in small (1-3 nm) Cu clusters after holding a constant potential at -0.93 V vs. RHE for 30 min. (k) *Operando* SERS of *CO adsorption on 3-5 nm or larger Cu nanograins showing the dominant feature at ~2050 cm^{-1} after holding the potential at -0.93 V for another 30 min.

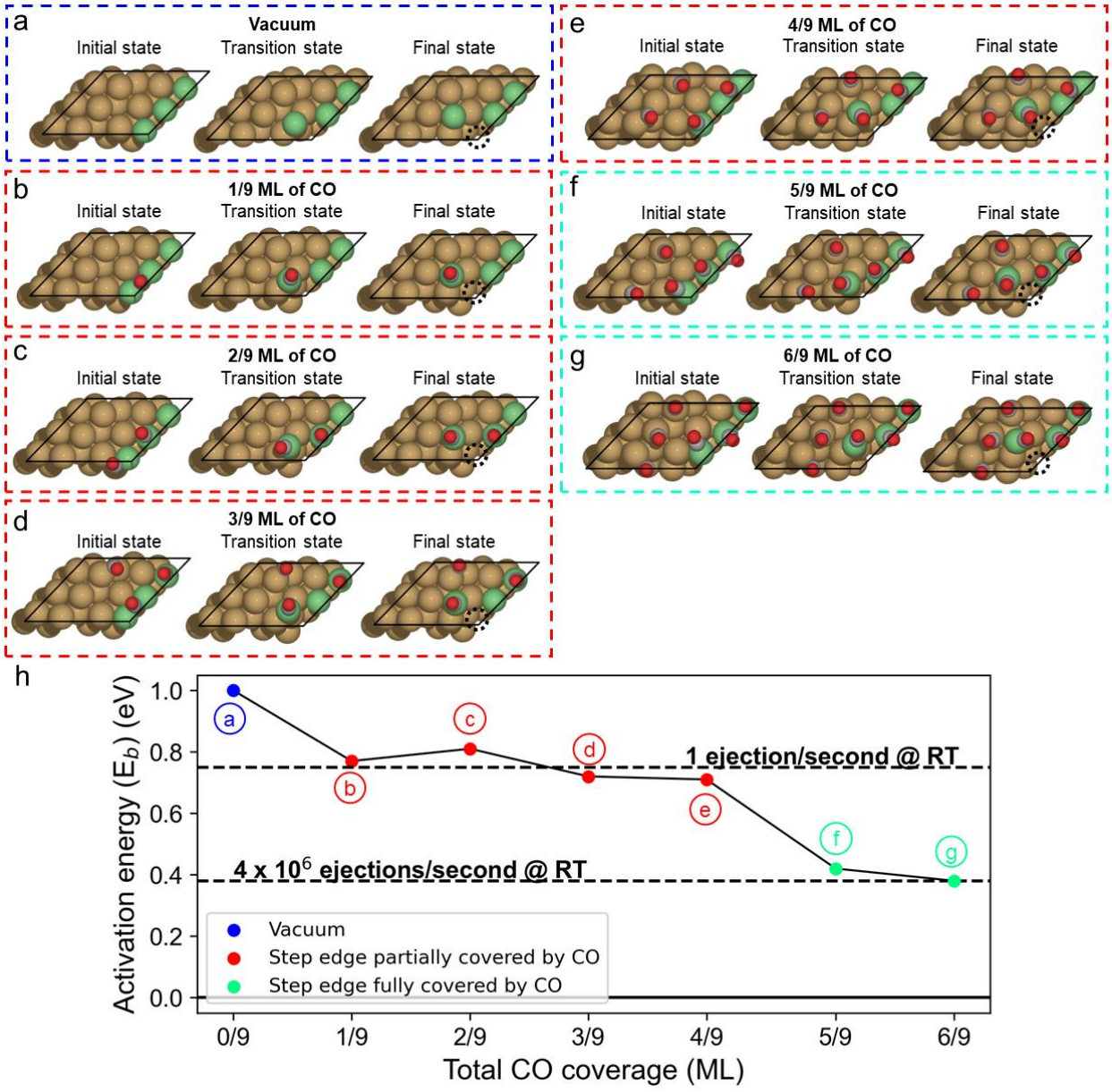

Figure 7. Calculated mechanisms and activation energy barriers for the ejection of Cu adatoms from Cu(511) as a function of CO coverage. a-g, Illustrations of the initial, transition, and final state of the lowest energy path for the ejection of a Cu atom from a Cu(511) step-edge under vacuum conditions (**a**) and in the presence of 1/9-6/9 ML of CO (**b-g**). (**h**) Calculated

activation energy barrier for the ejection of a Cu atom from the Cu(511) step edge as a function of CO coverage. The letter (**a-g**) used to label each activation energy barrier data point corresponds to the respective label in the illustrated cases (**a-g**). The horizontal dashed lines correspond to the required activation energy barrier to obtain a given rate (ejection per second) for Cu atom ejection at room temperature (RT). The top and bottom dashed lines correspond to a barrier of 0.75 eV and 0.38 eV respectively, leading to a rate of 1 and ~$4 \cdot 10^6$ events$\cdot s^{-1}$. Brown, green, gray, and red spheres in the insets represent Cu, surface step-edge Cu atoms, carbon, and oxygen atoms, respectively.

References:

1. Mariano, R. G., McKelvey, K., White, H. S. & Kanan, M. W. Selective increase in CO_2 electroreduction activity at grain-boundary surface terminations. *Science* **358**, 1187–1192 (2017).
2. Mefford, J. T. *et al.* Correlative operando microscopy of oxygen evolution electrocatalysts. *Nature* **593**, 67–73 (2021).
3. Yang, Y. *et al.* Electrocatalysis in Alkaline Media and Alkaline Membrane-Based Energy Technologies. *Chem. Rev.* **122**, 6117–6321 (2022).
4. Ross, M. B. *et al.* Designing materials for electrochemical carbon dioxide recycling. *Nat. Catal.* **2**, 648–658 (2019).
5. Birdja, Y. Y. *et al.* Advances and challenges in understanding the electrocatalytic conversion of carbon dioxide to fuels. *Nat. Energy* **4**, 732–745 (2019).
6. Wu, Y., Jiang, Z., Lu, X., Liang, Y. & Wang, H. Domino electroreduction of CO_2 to methanol on a molecular catalyst. *Nature* **575**, 639–642 (2019).
7. Zhu, P. *et al.* Continuous carbon capture in an electrochemical solid-electrolyte reactor. *Nature* **618**, 959–966 (2023).
8. Yang, Y. *et al.* Operando studies reveal active Cu nanograins for CO_2 electroreduction. *Nature* **614**, 262–269 (2023).
9. Feijóo, J. *et al. Operando* high-energy-resolution X-ray spectroscopy of evolving Cu nanoparticle electrocatalysts for CO_2 Reduction. *J. Am. Chem. Soc.* **145**, 20208–20213 (2023).
10. Yang, Y. *et al. Operando* electrochemical liquid-cell scanning transmission electron microscopy (EC-STEM) studies of evolving Cu nanocatalysts for CO_2 electroreduction. *ACS Sustain. Chem. Eng.* **11**, 4119–4124 (2023).
11. Chen, P.-C. *et al.* Chemical and Structural evolution of AgCu catalysts in electrochemical CO_2 reduction. *J. Am. Chem. Soc.* **145**, 10116–10125 (2023).
12. Lian, Z., Dattila, F., López, N. Stability and lifetime of diffusion-trapped oxygen in oxide-derived copper CO_2 reduction electrocatalysts. *Nat. Catal.* **7**, 401-411 (2024).
13. Huang, J. Hormann, N., Oveisi, E., Louidice, E., De Gregorio, G. L., Andreussi, O., Marzari, N., Buonsanti, R. Potential-induced nanoclustering of metallic catalysts during electrochemical CO_2 reduction. *Nat. Commun.* **9**, 3117 (2018).
14. Grosse, P., Yoon, A., Rettenmaier, C., Herzog, A., Chee, S. W., Roldan Cuenya, B. Dynamic transformation of cubic copper catalysts during CO_2 electroreduction and its impact on catalytic selectivity. *Nat. Commun.* **12**, 6736 (2021).

15. Lee, S. H. *et al.* Oxidation state and surface reconstruction of Cu under CO_2 reduction conditions from *in situ* X-ray characterization. *J. Am. Chem. Soc.* **143**, 588–592 (2021).
16. Takahashi, I., Koga, O., Hoshi, N. & Hori, Y. Electrochemical reduction of CO_2 at copper single crystal Cu(S)-[n(111)×(111)] and Cu(S)-[n(110)×(100)] electrodes. *J. Electroanal. Chem.* **533**, 135–143 (2002).
17. Hori, Y., Takahashi, I., Koga, O. & Hoshi, N. Selective formation of C2 compounds from electrochemical reduction of CO_2 at a series of copper single crystal electrodes. *J. Phys. Chem. B* **106**, 15–17 (2002).
18. Eren, B., Weatherup, R. S., Liakakos, N., Somorjai, G. A. & Salmeron, M. Dissociative carbon dioxide adsorption and morphological changes on Cu(100) and Cu(111) at ambient pressures. *J. Am. Chem. Soc.* **138**, 8207–8211 (2016).
19. Eren, B. *et al.* Activation of Cu(111) surface by decomposition into nanoclusters driven by CO adsorption. *Science* **351**, 475–478 (2016).
20. Xu, L. *et al.* Formation of active sites on transition metals through reaction-driven migration of surface atoms. *Science* **380**, 70–76 (2023).
21. Arán-Ais, R. M., Scholten, F., Kunze, S., Rizo, R. & Roldan Cuenya, B. The role of in situ generated morphological motifs and Cu(i) species in C_{2+} product selectivity during CO_2 pulsed electroreduction. *Nat. Energy* **5**, 317–325 (2020).
22. Kim, J. *et al.* Revealing CO_2 dissociation pathways at vicinal copper (997) interfaces. *Nat. Commun.* **14**, 3273 (2023).
23. Amirbeigiarab, R. *et al.* Atomic-scale surface restructuring of copper electrodes under CO_2 electroreduction conditions. *Nat. Catal.* **6**, 837–846 (2023).
24. Kim, Y.-G., Baricuatro, J. H., Javier, A., Gregoire, J. M. & Soriaga, M. P. The evolution of the polycrystalline copper surface, first to Cu(111) and then to Cu(100), at a fixed CO_2RR potential: a study by *operando* EC-STM. *Langmuir* **30**, 15053–15056 (2014).
25. Kim, Y.-G. *et al.* Surface reconstruction of pure-Cu single-crystal electrodes under CO-reduction potentials in alkaline solutions: A study by seriatim ECSTM-DEMS. *J. Electroanal. Chem*. **780**, 290–295 (2016).
26. Simon, G. H., Kley, C. S. & Roldan Cuenya, B. Potential-dependent morphology of copper catalysts during CO_2 electroreduction revealed by in situ atomic force microscopy. *Angew. Chem. Int. Ed.* **60**, 2561–2568 (2021).
27. Zelinski N. D., De la métallisation des organisms. *C.R. Acad. Sci. Paris.* **177**, 1041 (1923).
28. Boomer, E. H., Morris, H. E. & Argue, G. H. Apparent formation of copper carbonyl. *Nature* **129**, 438–438 (1932).
29. Robinson, P. L. & Stainthorpe, K. R. Two new carbonyls: copper and tellurium. *Nature* **153**, 24–25 (1944).
30. Kösy, F. A Volatile compound of copper. *Nature* **160**, 21–21 (1947).
31. Bloom, H. Evidence for the formation of a copper carbonyl. *Nature* **159**, 539–539 (1947).
32. Huber, H., Kuendig, E. P., Moskovits, M. & Ozin, G. A. Binary copper carbonyls. Synthesis and characterization of tricarbonylcopper, dicarbonylcopper, monocarbonylcopper, and hexacarbonyldicopper. *J. Am. Chem. Soc.* **97**, 2097–2106 (1975).

33. Alikhani, M. E. & Manceron, L. The copper carbonyl complexes revisited: Why are the infrared spectra and structures of copper mono and dicarbonyl so different? *J. Mol. Spectrosc.* **310**, 32–38 (2015).
34. Li, M. *et al.* Thermal stability of size-selected copper nanoparticles: Effect of size, support and CO_2 hydrogenation atmosphere. *Appl. Surf. Sci.* **510**, 145439 (2020).
35. Vavra, J. *et al.* Solution-based Cu+ transient species mediate the reconstruction of copper electrocatalysts for CO_2 reduction. *Nat. Catal.* (2024) doi:10.1038/s41929-023-01070-8.
36. Chen, C. *et al.* Highly crystalline multimetallic nanoframes with three-dimensional electrocatalytic surfaces. *Science* **343**, 1339–1343 (2014).
37. Xia, Y. *et al.* One-dimensional nanostructures: synthesis, characterization, and applications. *Adv. Mat.* **15**, 353–389 (2003).
38. Kongkanand, A. & Mathias, M. F. The Priority and challenge of high-power performance of low-platinum proton-exchange membrane fuel cells. *J. Phys. Chem. Lett.* **7**, 1127–1137 (2016).
39. Arán-Ais, R. M. *et al.* Identical location transmission electron microscopy imaging of site-selective Pt nanocatalysts: electrochemical activation and surface disordering. *J. Am. Chem. Soc.* **137**, 14992–14998 (2015).
40. Beermann, V. *et al.* Real-time imaging of activation and degradation of carbon supported octahedral Pt–Ni alloy fuel cell catalysts at the nanoscale using *in situ* electrochemical liquid cell STEM. *Energy Environ. Sci.* **12**, 2476–2485 (2019).
41. Williamson, M. J., Tromp, R. M., Vereecken, P. M., Hull, R. & Ross, F. M. Dynamic microscopy of nanoscale cluster growth at the solid–liquid interface. *Nat. Mater* **2**, 532–536 (2003).
42. Yang, Y. *et al. Operando* methods in electrocatalysis. *ACS Catal.* **11**, 1136–1178 (2021).
43. Yang, Y. *et al.* Operando methods: A new era of electrochemistry. *Curr. Opin. Electrochem.* **42**, 101403 (2023).
44. Yang, Y., Shao, Y.-T., DiSalvo, F. J., Muller, D. A. & Abruña, H. D. Metal monolayers on command: underpotential deposition at nanocrystal surfaces: a quantitative *operando* electrochemical transmission electron microscopy study. *ACS Energy Lett.* **7**, 1292–1297 (2022)
45. Pankhurst, J. R., Iyengar, P., Loiudice, A., Mensi, M., Buonstanti, R. Metal-ligand Bond strength determines the fate of organic ligands on the catalyst surface during the electrochemical CO_2 reduction reaction. *Chem. Sci.* **11**, 9296-9302 (2020).
46. Shan, Y. Nanometre-resolved observation of electrochemical microenvironment formation at the nanoparticle-ligand interface. *Nat. Catal*. **7**, 422-431 (2024).
47. Yang, Y. *et al.* Elucidating cathodic corrosion mechanisms with *operando* electrochemical transmission electron microscopy. *J. Am. Chem. Soc.* **144**, 15698–15708 (2022).
48. Yang, Y., Shi, C., Feijoo, J., Jin, J., Chen, C., Han, Y., Yang, P. Dynamic Evolution of Copper Nanowires during CO_2 Reduction Probed by Operando Electrochemical 4D-STEM and X-ray Spectroscopy. *J. Am. Chem. Soc*. **146**, 23398-23405 (2024).
49. Shi, C. *et al.* Uncovering material deformations via machine learning combined with four-dimensional scanning transmission electron microscopy. *npj Comput. Mater.* **8**, 114 (2022).
50. Shi, C. *et al.* Domain-dependent strain and stacking in two-dimensional van der Waals ferroelectrics. *Nat. Commun.* **14**, 7168 (2023).

51. Voyles, P. M. & Muller, D. A. Fluctuation microscopy in the STEM. *Ultramicroscopy* **93**, 147–159 (2002).
52. Yang, Y. *et al. Operando* resonant soft X-ray scattering studies of chemical environment and interparticle dynamics of Cu nanocatalysts for CO_2 electroreduction. *J. Am. Chem. Soc.* **144**, 8927–8931 (2022).
53. De Ruiter, J. An, H., Wu, L., Gijsberg, Z., Yang, S., Hartman, T., Weckhuysen, B., van der Stam, W. Probing the dynamics of low-overpotential CO_2 -to-CO activation on copper electrodes with time-resolved Raman spectroscopy. *J. Am. Chem. Soc.* **144**, 15047-15058 (2022).
54. Weng, Z., Wu, Y., Wang, M., Jiang, J., Yang, K., Huo, S., Wang, X., Ma, Q., Brudvig, G. W., Batista, V. S., Liang, Y., Feng Z., Wang, H. Active sites of copper-complex catalytic materials for electrochemical carbon dioxide reduction. *Nat. Commun*. **9**, 415 (2018).
55. Timoshenko, J. et al. Reversible metal cluster formation on Nitrogen-doped carbon controlling electrocatalyst particle size with subnanometer accuracy. *Nat. Commun*. **15**, 6111 (2024).
56. Zhang, L., Yang, X., Yuan, Q., Wei, Z., Ding, J., Chu, T., Rong, C., Zhang, Q., Ye, Z., Xuan, F.-Z., Zhai, Y., Zhang, B. Yang, X. Elucidating the structure-stability relationship of Cu single-atom catalysts using *operando* surface-enhanced infrared absorption spectroscopy. *Nat. Commun*. **14**, 8311 (2023).
57. Spiro, T. G., Soldatov, A. V., Balakrishnan, G. CO, NO and O_2 as vibrational probes of heme protein interactions. *Coord. Chem. Rev.* 257. 511-527 (2013).
58. Li, J., Li, X., Gunathunge, C. M., Waegele, M. M. Hydrogen bonding steers the product selectivity of electrocatalytic CO reduction. *Proc. Natl. Acad. Sci.* **116,** 9220-9229 (2019).
59. Hollins, P. The influence of surface defects on the infrared spectra of adsorbed species. *Surf. Sci. Rep.* **16**, 51-94 (1992).
60. Gunathunge, C. M., Li, X., Li, J., Hicks, R. P., Ovalle, V. J., Waegele, M. M. Spectroscopic Observation of Reversible Surface Reconstruction of Copper Electrodes under CO_2 Reduction. *J. Phys. Chem. C* **121**, 12337-12344 (2017).
61. An, H., et al. Sub-Second Time-Resolved Surface-Enhanced Raman Spectroscopy Reveals Dynamic CO Intermediates during Electrochemical CO_2 Reduction on Copper. *Angew. Chem. Int. Ed*. 60, 16576 (2021).
62. Liu, S. Alkali cation-induced cathodic corrosion in Cu electrocatalysts. *Nat. Commun*. **15**, 5080 (2024).
63. Hersbach, T. J. P., Koper, M. T. M. Cathodic corrosion: 21st century insights into a 19th century phenomenon. *Curr. Opin. Electrochem*. **26**, 100653 (2021).
64. Louisia, S. *et al.* The presence and role of the intermediary CO reservoir in heterogeneous electroreduction of CO_2. *Proc. Natl. Acad. Sci.* **119**, e2201922119 (2022).
65. Xu L., Mavrikakis M., Structure sensitivity in adsorbate-induced adatom formation on fcc transition-metal surfaces. *J. Catal.* **31**, 115373 (2024).
66. Förster, S., Apostol, L., Bras, W. Scatter: Software for the analysis of nano- and mesoscale small-angle scattering. *J. Appl. Crystallogr*. **43**, 639-646 (2010).
67. McInnes, L., Healy, J., Saul, N., Großberger, L. UMAP: Uniform Manifold Approximation and Projection. *J Open Source Softw*. **3**, 861 (2018).

68. Hartigan, J. A., Wong, M. A. K-Means clustering algorithm. *J Royal Statistical Soc. Ser C Appl. Statistics* **28**, 100–108 (1979).
69. Kresse, G., Furthmüller, J. Efficient iterative schemes for ab initio total-energy calculations using a plane-wave basis set, *Phys. Rev. B.* **54**, 11169-11186 (1996).
70. Kresse, G., Furthmüller, J. Efficiency of ab-initio total energy calculations for metals and semiconductors using a plane-wave basis set, *Comput. Mater. Sci.* **6**, 15-50 (1996).
71. Perdew, P., Burke, K., Ernzerhof, M. Generalized gradient approximation made simple. *Phys. Rev. Lett.* **77**, 3865-3868 (1996).
72. Blöchl, P. E. Projector augmented-wave method, *Phys. Rev. B.* **50**, 17953-17979 (1994).
73. Monkhorst, H., Pack, J. Special points for Brillouin-zone integrations, *Phys. Rev. B.* **13**, 5188-5192 (1976).
74. Neugebauer, J., Scheffler, M. Adsorbate-Substrate and adsorbate-adsorbate interactions of Na and K adlayers on Al (111). *Phys. Rev. B.* **46**, 16067-16080 (1992).
75. Bengtsson, L. Dipole correction for surface supercell calculations. *Phys. Rev. B.* **59**, 12301-12304 (1999).
76. CRC Handbook of Chemistry and Physics, 94th Edition, 2014.
77. Henkelman, G., Uberuaga, B. P., Jonsson, H. A Climbing image nudged elastic band method for finding saddle points and minimum energy paths. *J. Chem. Phys.* **113**, 9901-9904 (2000).